


Optical resonances in graded index spheres: A resonant-state-expansion study and analytic approximations

Z. Sztranyovszky , W. Langbein, and E. A. Muljarov

School of Physics and Astronomy, Cardiff University, Cardiff CF24 3AA, United Kingdom



(Received 22 September 2021; accepted 22 February 2022; published 25 March 2022)

Recent improvements in the resonant-state expansion (RSE), focusing on the static mode contribution, have made it possible to treat transverse-magnetic (TM) modes of a spherically symmetric system with the same efficiency as their transverse-electric (TE) counterparts. We demonstrate here that the efficient inclusion of static modes in the RSE results in its quick convergence to the exact solution regardless of the static mode set used. We then apply the RSE to spherically symmetric systems with continuous radial variations of the permittivity. We show that in TM polarization, the spectral transition from whispering gallery to Fabry-Pérot modes is characterized by a peak in the mode losses and an additional mode as compared to TE polarization. Both features are explained quantitatively by the Brewster angle of the surface reflection which occurs in this frequency range. Eliminating the discontinuity at the sphere surface by using linear or quadratic profiles of the permittivity modifies this peak and increases the Fabry-Pérot mode losses, in qualitative agreement with a reduced surface reflectivity. These profiles also provide a nearly parabolic confinement for the whispering gallery modes, for which an analytical approximation using the Morse potential is presented. Both profiles result in a reduced TE-TM splitting, which is shown to be further suppressed by choosing a profile radially extending the mode fields. Based on the concepts of ray optics, phase analysis of the secular equation, and effective quantum-mechanical potential for a wave equation, we discuss a number of useful approximations which shed light on the physical phenomena observed in the spectra of graded-index systems.

DOI: [10.1103/PhysRevA.105.033522](https://doi.org/10.1103/PhysRevA.105.033522)

I. INTRODUCTION

Modeling inhomogeneous optical resonators is challenging, as generally a simple analytic solution is not available. A special case are spherically symmetric systems, having an inhomogeneity, for example, in the permittivity, only dependent on the radius. Examples can be found in core-shell systems which allow highly directional scattering [1], when modeling surface contamination on a sphere due to diffusion [2] or high pressure [3], or when modeling biological cells [4]. Graded index profiles can be used to engineer the cancellation of electric and magnetic dipole excitation, which reduces the visibility of small particles at certain wavelengths [5]. With an inhomogeneous and anisotropic sphere, one can even achieve perfect cloaking of a cavity over a range of frequencies [6]. On a larger scale, one may use inhomogeneous profiles to model emission from stellar atmospheres [7].

The scattering properties of systems with graded permittivity have been studied in the literature using various approximate methods. In the multilayer approach (also referred to as stratified medium method), the graded index profile is approximated by a piecewise constant function, describing the system by homogeneous regions comprising a core covered by a sequence of shells [8,9]. In the short wavelength limit, a Debye series expansion for the scattered field was used [10], and in the long wavelength limit a Born approximation [11] or a dipole limit [5] was applied to dispersive systems with complex permittivity. Furthermore, the

dipole moment of dielectric spherical particles with power law radial profiles of the permittivity was calculated in the electrostatic limit [12]. A generalized scattered field formulation developed in Ref. [2] requires solving scalar Schrödinger-like equations, similar to the scalar wave equations solved in this paper. To study the electromagnetic (EM) modes, first- and second-order perturbation methods were developed [13] and applied to deformations of a homogeneous sphere [14]. Whispering gallery (WG) modes in both transverse-electric (TE) and transverse-magnetic (TM) polarizations were studied in Ref. [3] for small inhomogeneous perturbations of the surface layer of a sphere. In that approach, the modes were found in the complex frequency plane based on the expansion coefficients of the generalized scattered field, and the secular equations were solved numerically using a Runge-Kutta method. The effect of a linearly changing permittivity profile was investigated in Ref. [15] for high-frequency TE modes in large spheres, using Airy functions as an approximate solution to the corresponding scalar problem. Finally, in Ref. [16], a resonant mode of a sphere was treated in the electrostatic limit for a negative and frequency-dependent permittivity, described by an undamped (i.e., nonabsorbing) Drude model, with radial dependencies of the permittivity and the electric field approximated by polynomials.

Here we will use the resonant-state expansion (RSE) to study the modes of graded index spherical resonators. The RSE is a rigorous theoretical method in electrodynamics for calculating the resonant states (RSs) of an arbitrary open

optical system [17]. Using the RSs of a basis system, which can be chosen to be analytically solvable, such as a homogeneous dielectric sphere in vacuum, the RSE determines the RSs of the target system by diagonalizing a matrix equation containing a perturbation. This perturbation is defined as the difference between the basis and target systems and is expressed as a change of the permittivity and permeability distributions with respect to the basis system [18].

For a general perturbation, one needs to include static modes [19,20] alongside the RSs in the Mittag-Leffler (ML) representation of the dyadic Green's function. Note that the latter is at the heart of the RSE approach. Recently, the RSE has been reformulated [21] to eliminate static modes, and the illustrations provided for perturbations of the size and refractive index of a homogeneous sphere show a significantly improved convergence compared to the original version of the RSE [20]. The approach [21] has also proposed, though without providing illustrations, another quickly convergent version of the RSE—the one which keeps static modes in the basis.

In this paper, we consider both versions of the reformulated RSE, with and without static modes, demonstrating a similar efficiency of both. Using the RSE, we then investigate spherically symmetric inhomogeneous systems with graded permittivity profiles. The RSs in such systems are still split into TE and TM polarizations and are characterized by the azimuthal (m) and angular (l) quantum numbers. Importantly, while some graded profiles are approximately solvable analytically [7,22], the RSE can treat arbitrary perturbations and finds all the RSs of the system within the spectral coverage of the basis used, thus generating a full spectrum. This allows us to identify some prominent features in spectra, such as the quasidegeneracy of modes and the Brewster angle phenomenon, and ultimately to engineer the shape of the spectrum via changing the permittivity profile.

The paper is organized as follows. In Sec. II, we study the TE and TM RSs of a homogeneous sphere, using the ray picture of light propagation as well as a more rigorous phase analysis of the secular equations describing the light eigenmodes, both approaches introducing several useful approximations. In Sec. III, we briefly describe the RSE method and its optimizations used here for calculating the RSs of a graded index sphere. We then recap the analogy between wave optics and quantum mechanics by introducing a radial Schrödinger-like wave equation containing an effective potential. The RSs of a sphere with linear and quadratic radial permittivity profiles eliminating the discontinuity at the sphere surface are then discussed, and an approximate analytical solution using Morse's potential is presented. In Sec. IV, we investigate the TE-TM RS splitting and its reduction for graded index profiles. Details of the calculations are provided in the Appendices, including a comparison of the performance of the two optimized versions of the RSE, with and without elimination of static modes.

II. HOMOGENEOUS SPHERE

The secular equation determining the RS wave number k_n of a nonmagnetic homogeneous sphere of radius R with

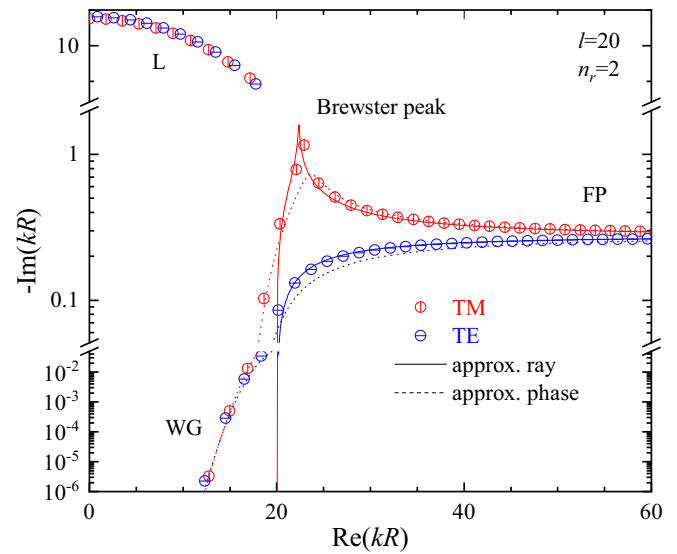


FIG. 1. Wave numbers of the TE and TM RSs of a homogeneous sphere in vacuum, with a refractive index of $n_r = 2$ and an angular momentum quantum number of $l = 20$. The regions of leaky modes (L), whispering gallery modes (WG), and Fabry-Pérot modes (FP) are indicated. Solid and dashed lines are the approximations to the imaginary part of the wave numbers, given by Eqs. (3) and (9), respectively. Note the double y-axis break.

vacuum outside is given by [21]

$$\frac{J'(n_r k_n R)}{J(n_r k_n R)} = \frac{1}{\beta} \frac{H'(k_n R)}{H(k_n R)}, \quad (1)$$

where $\beta = n_r$ ($\beta = n_r^{-1}$) for TE (TM) polarization. Here $J(x) = x j_l(x)$ and $H(x) = x h_l^{(1)}(x)$, with j_l and $h_l^{(1)}$ being, respectively, the spherical Bessel function and Hankel function of the first kind, and primes denote the first derivatives of functions with respect to their arguments. Figure 1 shows the spectrum of the RSs of a homogeneous dielectric sphere in vacuum in the complex wave-number plane for a refractive index of the sphere of $n_r = 2$ and an angular momentum quantum number of $l = 20$. For the example given, the combination of parameters n_r and l are chosen such that the spectrum contains a few WG modes. Here, $k = 2\pi/\lambda_0$ is the wave number in vacuum, and λ_0 is the wavelength of light in vacuum. Only $\text{Re } k \geq 0$ is shown, noting that RSs come in pairs with both signs of the real part of their wave number. The spectrum consist of TE and TM modes which appear in alternating order, with one exception related to the Brewster's angle phenomenon, as discussed later. The RSs of a sphere can be divided into three groups: leaky (L) modes, WG modes, and Fabry-Pérot (FP) modes. Physically, all of them are formed as a result of interference of EM waves interacting with the sphere surface.

L modes typically have quality factors (Q factors) which are very low, and their EM fields are located mainly outside the sphere. The number of L modes is exactly l in TE and $l - 1$ in TM polarization, although the Brewster mode discussed later can be regarded as a hybrid L-FP mode, so that the number of L modes is effectively the same in both polarizations. For comparison, the case of $l = 5$, with the

same refractive index n_r , can be seen in Ref. [19]. L modes arrange around the origin in the complex wave-number plane, forming a roughly semicircular arc.

WG modes are formed due to the total internal reflection and therefore have wave numbers with $|\text{Re } k| < l/R$, as discussed below. The number of WG modes increases with n_r and l . The Q factor of the fundamental WG mode increases exponentially with l , and values of up to 10^{10} , only limited by material properties, have been demonstrated experimentally [23]. The EM field of the WG modes is concentrated inside the sphere close to the surface.

FP modes of a sphere have moderate Q factors and are named for their similarity to the original FP modes [24] of a double-mirror planar resonator. In fact, at large frequency, the FP modes of a sphere approach the limit of an equidistant spectrum of a dielectric slab, with all the eigenfrequencies having the same imaginary part [17]. The number of FP modes is countable infinite. Their EM fields are distributed within the sphere, avoiding the center due to the nonzero angular momentum ($l > 0$). The FP modes are spectrally separated from the WG modes by the critical angle of the total internal reflection, as discussed in more depth later.

The arrangement of the RSs in Fig. 1 is overall similar in the TE and TM polarizations. The imaginary part of their wave numbers approaches the same high frequency asymptote, albeit from opposite sides. Additionally, there is a peak in the imaginary part of the TM RS wave numbers near the transition region from WG to FP modes, which occurs around the Brewster angle in the ray picture of light propagation, and we therefore refer to it as a Brewster peak. At this peak, an additional TM mode is formed, breaking the otherwise alternating order of TE and TM RSs.

Let us now discuss and analyze the spectrum of the RSs of a sphere in more detail, using two different approaches: the ray picture and a phase analysis. Both approaches provide some useful approximations for the mode positions and line widths and offer an intuitive understanding of the origin and properties of the RSs of a sphere.

A. Ray picture: Brewster's phenomenon and total internal reflection

To understand the observation of the Brewster peak in the spectrum of the RSs, we recall that increasing the angle of light incidence θ at a planar interface between two media, the Fresnel reflection coefficient for TM (aka p) polarized light passes through zero, changing its sign at the Brewster angle [25]. The same occurs at the surface of a sphere in the ray picture, which is valid in the limit of wavelengths much smaller than the surface curvature. This local geometry is illustrated in the inset of Fig. 2. The magnitude of the incident wave vector is $n_1 k$, where n_1 is the refractive index of the corresponding medium, i.e., that of the sphere, $n_1 = n_r$. Since the angular momentum l gives the number of wave periods along one circumference $2\pi R$, the wave vector component p parallel to the surface is determined by $2\pi l = 2\pi R p$, so $p = l/R$. With simple trigonometry, we can see that $\sin \theta = p/(n_1 k)$. The Brewster angle θ_b is determined by $\tan \theta_b = n_2/n_1$, so for a sphere in vacuum ($n_2 = 1$), the wave number corresponding

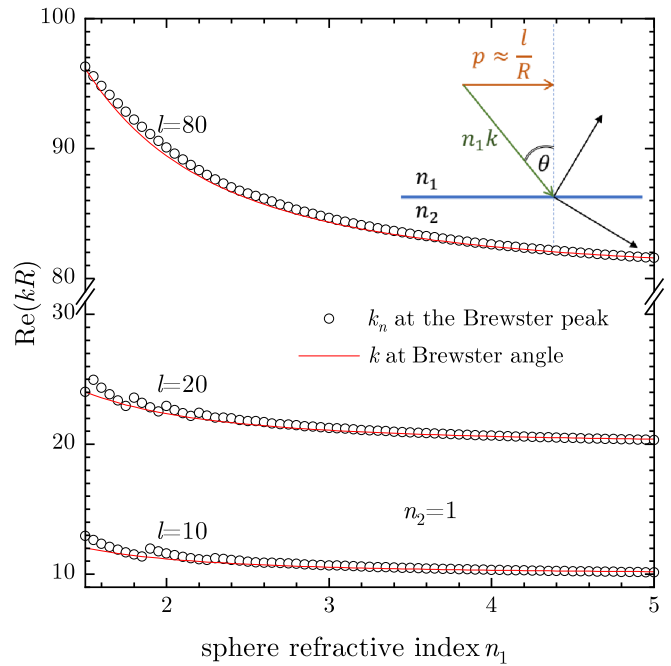


FIG. 2. Real part of the wave number of the TM RS at the Brewster peak (circles) as a function of the sphere refractive index $n_1 = n_r$, for $l = 10$, $l = 20$, and $l = 80$, compared with the ray optics approximation Eq. (2) (lines). Inset: Sketch of the ray geometry at the boundary.

to the Brewster angle is given by

$$k_b = \frac{l}{R} \sqrt{\frac{1}{n_1^2} + 1}. \quad (2)$$

At this angle, the reflectivity vanishes. This would correspond to a divergence of the imaginary part of the RS wave number for an ideal planar geometry. Here instead, it is kept finite due to the finite curvature of the surface and the RS discretization, resulting in the Brewster peak.

In Fig. 2, we compare Eq. (2) with the real part of the wave number of the Brewster mode (the TM mode at the Brewster peak in the spectrum), for $l = 10$, $l = 20$, and $l = 80$, all showing good agreement. We find that the relative error for small n_1 increases with decreasing l . For smaller l , the peak position shifts to longer wavelength, and the ratio of internal wavelength to the radius increases, therefore the validity of the ray picture reduces. With increasing n_1 , the RSs are packed more densely in the complex k plane, so the discretization does not result in significant deviations. At the same time, the light wavelength within the sphere $2\pi/(n_1 k)$ decreases with n_1 , thus improving the accuracy of the ray picture.

The Brewster mode can also be associated with the leaky branch. In fact, as n_1 increases, the Brewster peak in the spectrum is getting sharper, so the Brewster mode is taking a significantly larger imaginary part of the wave number compared to the neighboring FP modes and is thus getting more isolated from them, at the same time approaching the edge of the leaky branch. Indications of this can be seen in Figs. 7 and 10 in the Appendix. We also note that for high l , the Brewster peak can be shifted further into the FP spectral region. This

happens because the Brewster angle θ_b is always smaller than the critical angle θ_c of the total internal reflection. The latter determines the point in the spectrum separating WG from FP modes and can be evaluated in a similar way, leading to $k_c = l/R$. Comparing it with Eq. (2), we see that as l increases or n_l decreases, the difference $k_b - k_c$ is getting larger, so the corresponding region in the spectrum between the critical and Brewster angles can accommodate more RSs.

The ray picture is also useful for understanding the imaginary part of the FP mode wave numbers. Assuming the reflectivity amplitude r_p at the sphere surface in polarization P is given by the corresponding Fresnel coefficient, we equate it to the ratio of the field amplitude before and after each reflection. This ratio is in turn given by the temporal decay of the field, $|r_p| = \exp(-t/\tau)$, where t is the time between consecutive reflections and τ is the mode decay time which is given by the imaginary part of its eigenfrequency, $1/\tau = -\text{Im}(kc)$. At the same time, the optical path length across the sphere between two reflections is given by $L = 2Rn_r \cos\theta$. Finally, using the fact that $t = L/c$ and taking the logarithm of the reflectivity results in

$$\text{Im } k = \frac{\ln |r_p|}{2Rn_r \cos\theta}, \quad (3)$$

where the Fresnel coefficient r_p depends on the angle of incidence θ and the refractive index of the sphere n_r . The expression is valid up to the critical angle θ_c of total internal reflection, at which $\ln |r_p| = 0$. The values obtained according to Eq. (3) are shown in Fig. 1 as solid lines. We can see good agreement for both polarizations, including the Brewster peak and the asymptotic value for FP modes, evaluated to $-0.27465/R$ for $n_r = 2$ and $\theta = 0$, which again validates the ray optics interpretation of the RS properties. The WG modes are located in the total internal reflection region of the spectrum where Eq. (3) is not applicable—their nonvanishing imaginary parts are the result of the finite curvature of the sphere making the reflection imperfect. We therefore consider in the following subsection an approximation (shown in Fig. 1 by dashed lines) which is based on the phase analysis of the secular equation determining the RSs.

B. Phase analysis: Mode positions and line widths

To develop a better understanding of the location of the modes in the complex plane given by k_n , we discuss here an approximate solution to the secular equation. For $|z| \gg l$, we can approximate the left-hand side of Eq. (1) as [26]

$$\frac{J'(z)}{J(z)} \approx -\tan\left(z - \frac{l+1}{2}\pi\right). \quad (4)$$

It is therefore useful to introduce the following two phase functions:

$$\Psi(k) = \text{atan}\left(-\frac{J'(n_r k R)}{J(n_r k R)}\right) \quad (5)$$

and

$$\Phi(k) = \text{atan}\left(-\frac{1}{\beta} \frac{H'(kR)}{H(kR)}\right). \quad (6)$$

Substituting them into Eq. (1) yields

$$\Psi(k_n) = \Phi(k_n) + n\pi, \quad (7)$$

where n is an arbitrary integer. For real k , it can be seen that $\Psi(k)$ is a real monotonous function (on a selected Riemann sheet), and according to Eq. (4) becomes linear at large k . At the same time, $\Phi(k)$ is complex even for real k , and its real part varies between $\pi/2$ and 0 monotonously (nonmonotonously) with k for TE (TM) polarization. The functions $\Psi(k) - n\pi$, and $\text{Re } \Phi(k)$ for TE and TM polarizations, are plotted in Fig. 6 in Appendix A, which allows a graphical solution of Eq. (7), namely, the intersections of the curves for $\Psi(k) - n\pi$ and $\text{Re } \Phi(k)$ determine the approximate positions of the modes in spectra. More rigorously, separating the real and the imaginary parts of the wave number, $k_n = k'_n + ik''_n$, the mode positions in the spectra, k'_n , are given by

$$\Psi(k'_n) - n\pi \approx \text{Re } \Phi(k'_n), \quad (8)$$

whereas k''_n , determining the mode line widths, by

$$k''_n \approx \frac{1}{n_r R} \text{Im } \Phi(k'_n), \quad (9)$$

in accordance with the asymptotic behavior Eq. (4).

The approximation Eq. (9) for the mode linewidth is illustrated in Fig. 1 by dashed lines, demonstrating a good agreement for WG and FP modes. While it is less accurate than Eq. (3) for most FP modes, it provides a suited approximation for the WG modes, where the latter fails. The accuracy provided by this approximation improves as the refractive index n_r of the sphere increases, as seen in Fig. 7 in Appendix A. Compared to Eq. (1.1) of Ref. [27], here Eq. (8) is not an explicit expression for the mode position, and the approximation Eq. (9) is less accurate than Eq. (1.3) of Ref. [27], but the graphical solution (Fig. 6) provides intuition into the emergence of the modes and the difference between the TE and TM polarizations.

Using the above phase analysis, one can also obtain an analytic approximation for the RS wave numbers in the large frequency limit, $n_r k R \gg l$. Using the fact that $\tan \Phi(k) \rightarrow -i/\beta$ at $k \rightarrow \infty$ and the asymptotic behavior of $\Psi(k)$ given by Eq. (4), one can evaluate

$$\begin{aligned} k_n^{\text{TE}} &\approx \frac{1}{2n_r R} \left[(2n + l + 1)\pi - i \ln \frac{n_r + 1}{n_r - 1} \right], \\ k_n^{\text{TM}} &\approx \frac{1}{2n_r R} \left[(2n + l + 2)\pi - i \ln \frac{n_r + 1}{n_r - 1} \right], \end{aligned} \quad (10)$$

where the integer n can be used to number the RSs. For a full derivation of Eq. (10), see Appendix A.

The RS wave numbers given by the approximation Eq. (10) are identical to those of a homogeneous slab at normal incidence [17]. The latter are in turn consistent with Eq. (3) used for the normal incidence reflection, which gives $\text{Im}(kR) = \ln[(n_r - 1)/(n_r + 1)]/(2n_r)$, as in Eq. (10). At nonnormal incidence, the TE and TM FP modes of a slab asymptotically converge to each other in pairs, as shown in Fig. 8 in Appendix B. The planar system gives rise to both even and odd modes (using the parity of the electric or magnetic field), with odd TE modes converging to even TM modes at large frequencies, and vice versa. In the sphere, however, there are

no even modes, as required by the finiteness of the EM field at the origin (as in any other point in space). Considering only the even modes of the slab spectra, we obtain the FP modes of the sphere, which alternate between TE and TM RSs with increasing $\text{Re}(k)$. This is consistent with the analytic approximation Eq. (10) and visible in the spectrum of the sphere presented in Fig. 1.

III. GRADED INDEX SPHERES

In this section, we study, using the RSE, the RSs in spherically symmetric nonmagnetic systems with graded permittivity profiles. A particularly interesting situation is reached by removing discontinuities of the permittivity. Here we study cases where the discontinuity is removed either only in the permittivity (linear case) or both in the permittivity and its derivative (quadratic case), and compare both cases with each other and with the constant permittivity profile studied in Sec. II. We note that removing discontinuities of the refractive index yields broadband antireflecting coatings in planar dielectric layers [28]. For the WG modes, we introduce a radial Schrödinger-like wave equation containing an effective potential, compare potentials and mode properties in all three cases, and provide an analytical approximation based on the Morse potential.

A. Calculating the resonances

1. Resonant-state expansion

Here we briefly discuss the methodology based on the RSE [19–21] which is used for the numerical calculations. The RSE is well suited for calculating the RSs of a graded index sphere. The difference in the permittivity between the target system (a graded index sphere) and the basis system (a constant index sphere) is treated as a perturbation, and the RSs of the constant index sphere serve as a basis for the RSE. The EM fields of the RSs of the target system are expanded into the basis RSs, and the expansion coefficients and the RS wave numbers of the target system are found by solving a linear eigenvalue problem, see Eq. (C1) in Appendix C. This eigenvalue problem of the RSE contains as input the RS wave numbers of the basis system and the matrix elements of the perturbation. For spherically symmetric systems TE and TM polarizations, or RSs with different l and magnetic quantum number m , do not mix and can be treated separately in RSE. However, the matrix elements used in the RSE for the TE and TM RSs are different, see Ref. [21] and Appendix C for details. In particular, for TM polarization, one needs to include in the basis additional functions which are required for completeness and physically describe the part of the EM field in a graded index sphere which is not divergence free. More rigorously, these functions are required to properly describe a longitudinal part of the dyadic GF related to its static pole in the ML expansion. Without these additional functions, the mode wave numbers calculated by the RSE carry a systematic error [20].

The RSE eigenvalue problem (see Appendix C) leads to an infinite matrix. For computational evaluation, this matrix is truncated to a finite size $N \times N$, where N is the number of RSs of the basis system used in the calculation. The specific RSs

used are the basis RSs having complex wave numbers with an absolute value below k_{max} .

Previously, the static pole of the GF in the ML expansion has been treated within the RSE by introducing a complete set of static modes [20]. However, even though the treatment of static modes is numerically less complex, a slow convergence versus the basis size N observed in Ref. [20] remained an issue. To develop quickly converging versions of the RSE, the full ML representation of the dyadic GF of a spherically symmetric system has been studied in Ref. [21], focusing, in particular, on the static pole of the GF containing a δ -like singularity. A quick convergence of the RSE has been achieved and demonstrated in Ref. [21] by an explicit isolation of the singularity that has allowed to avoid its direct expansion into static modes. Two ML forms of the GF have been introduced in Ref. [21], called there ML3 and ML4, which led to slightly different versions of the RSE, both quickly convergent to the exact solution.

The quick convergence of the RSE based on ML4, with static mode elimination and suited only for a basis system in a form of a homogeneous sphere, was demonstrated in Ref. [21] on examples of both size and material (strength) perturbations of a sphere. However, the version of the RSE based on ML3, which is using explicitly a static mode set and an arbitrary spherically symmetric basis system, has not been studied so far numerically. Such a study is given in Appendix C, including a comparison with ML4, demonstrating a similar level of convergence. We show there, in particular, that the RSE based on ML3 and ML4 both have a quick $1/N^3$ convergence to the exact solution, where N is the basis size of the RSE. Furthermore, taking three different static mode sets introduced earlier in Refs. [20,21], we show in Appendix C that the results of the RSE based on ML3 are similar for all the different static mode sets previously suggested.

Let us finally note that for perturbations without discontinuities, the above-mentioned optimization of the RSE might be not needed, as demonstrated in a similar approach based on eigenpermittivity modes [29]. However, as we are going to consider a transformation of an optical system from a homogeneous sphere, having a discontinuity, to a sphere with a continuous permittivity profile, the perturbation describing this transformation and used in RSE contains a discontinuity, both in linear and quadratic cases, and therefore the above optimization is in fact needed.

In all calculations of the RSs of the graded index spheres done in this paper, we use the RSE based on ML4, as it has a fixed number of additional basis functions in TM polarization, which is three times the number of the TM RSs included in the basis. We use a basis size of $N = 800$ (reached at $k_{\text{max}}R \approx 600$) in both cases of linear and quadratic profiles, which provides a relative accuracy better than 10^{-6} , as exemplified in Figs. 9 and 10.

2. Quantum-mechanical analogy—the effective potential

To intuitively understand the properties of the RSs in graded-index optical systems, it is useful to consider the analogy between Maxwell's and Schrödinger's wave equations and to introduce an effective optical potential [30]. In spherically symmetric systems, all the components of the

electric and magnetic fields can be expressed in terms of a radially dependent scalar field [21]. For TE (TM) polarization, this is the magnitude of the electric (magnetic) field, which has only a tangential component $E(r) = \mathcal{E}(r)/r$ ($H(r) = -i\mathcal{H}(r)/r$). For nonmagnetic systems, with the radial permittivity profile $\varepsilon(r)$ and permeability $\mu(r) = 1$, the scalar field $\mathcal{E}(r)$ satisfies the Schrödinger-like equation [21]

$$\left(\frac{d^2}{dr^2} - \frac{\alpha^2}{r^2} + k^2 \varepsilon(r) \right) \mathcal{E}(r) = 0, \quad (11)$$

where $\alpha = \sqrt{l(l+1)}$. In fact, assuming a particle mass $M = \hbar^2/2$, Eq. (11) can be interpreted as a quantum-mechanical analog (QMA). An obvious limitation of this QMA is that k^2 , playing the role of the complex eigenvalue for the RSs, contributes to Eq. (11) not in the same way as the energy in Schrödinger's equation. Associating k^2 with the particle energy, and using the fact that $\varepsilon(r) = 1$ (or a constant) outside the system, Johnson [30] introduced an energy-dependent effective potential, which makes the analogy with quantum mechanics no so straightforward. Here instead, we interpret Eq. (11) as an equation for the *zero-energy* state of a particle in a one-dimensional potential

$$V^{\text{TE}}(r) = -k^2 \varepsilon(r) + \frac{\alpha^2}{r^2}, \quad (12)$$

in which k plays the role of a complex parameter of the potential. In this QMA, every RS of the optical system, described by the wave function $\mathcal{E}(r)$, has zero quantum-mechanical energy and a potential Eq. (12) valid for this RS only, given by the corresponding value of k .

Likewise, for TM polarization, the scalar field $\mathcal{H}(r)$ satisfies an equation [21]

$$\left(-\frac{1}{\varepsilon(r)} \frac{d\varepsilon}{dr} \frac{d}{dr} + \frac{d^2}{dr^2} - \frac{\alpha^2}{r^2} + k^2 \varepsilon(r) \right) \mathcal{H}(r) = 0, \quad (13)$$

again, valid for a nonmagnetic system described by the permittivity $\varepsilon(r)$. Compared to Eq. (11), there is an additional term proportional to the logarithmic derivative of the permittivity, which can be included in the potential, yielding

$$V^{\text{TM}}(r) = V^{\text{TE}}(r) + \frac{\varepsilon'(r) \mathcal{H}'(r)}{\varepsilon(r) \mathcal{H}(r)}, \quad (14)$$

where the prime indicates the spatial derivative. The second term in Eq. (14) is analyzed and discussed in more depth in Sec. IV A. This helps the understanding of the TE-TM mode splitting. Here, we only note that this term, in its above form depending on the wave function, is inconsistent with the standard definition of the potential. However, introducing a rescaled wave function $\tilde{\mathcal{H}}(r) = \sqrt{\varepsilon(r)} \mathcal{H}(r)$ brings the effective potential to the form

$$\tilde{V}^{\text{TM}}(r) = V^{\text{TE}}(r) + \frac{3}{4} \left[\frac{\varepsilon'(r)}{\varepsilon(r)} \right]^2 - \frac{1}{2} \frac{\varepsilon''(r)}{\varepsilon(r)}, \quad (15)$$

which is now independent of the wave function, thus providing a valid QMA also for TM polarization, as detailed in Appendix D.

Note that the radial equations (11) and (13) are aligned with the standard Maxwell boundary conditions requiring that \mathcal{E} and \mathcal{E}' are continuous in TE polarization, and \mathcal{H} and \mathcal{H}'/ε are

continuous in TM polarization. Clearly, any discontinuity of ε results in \mathcal{H}' being also discontinuous in TM polarization, which is, in particular, the case of a homogeneous dielectric sphere in vacuum. We note that one can find the eigenmodes of graded index spheres by solving the radial equations directly with an appropriate numerical method. However, this approach does not guarantee that all modes in a region of interest in the complex plane are found. In this paper, we therefore use the effective potential picture only for qualitative discussions and for developing an approximation based on the Morse potential.

B. Graded index permittivity profiles

1. Constant permittivity

The TE and TM modes of a homogeneous sphere in vacuum, used as basis system in the RSE and described by a constant permittivity

$$\varepsilon(r) = 1 + A\theta(R - r), \quad (16)$$

where $\theta(x)$ is the Heaviside function and $A = n_r^2 - 1$, are shown in Fig. 3(a) for $n_r = 2$ (note they are the same as in Fig. 1). The fields, $\mathcal{E}(r)$ and $\mathcal{H}(r)$, and the corresponding effective potentials, given by Eqs. (12) and (14), are illustrated in Fig. 3(b) for the fundamental WG mode for TE and TM polarizations respectively. Both potentials decrease with radius due to the centrifugal term α^2/r^2 and have similar steplike barriers at the sphere surface ($r = R$) due to the step in the permittivity. In the TM potential, there is additionally a δ function at the sphere surface due to the derivative of the permittivity, see Eq. (14). The fields are effectively confined near the sphere surface, on one side by the centrifugal term increasing toward the center of the sphere and on the other side by the refractive index step at the sphere surface. The fields have evanescent tails extending outside of the sphere, which convert at larger distances into propagating waves once the potentials become negative, and then grow exponentially due to the imaginary part of the potentials created by the complex k .

The optical transmission through the barrier determines the losses of the WG modes and hence the imaginary part of their wave numbers. The height of the barrier depends on the size of the permittivity step and the angular quantum number l , and the transmission reduces about exponentially with l , thus allowing for very low mode losses [31]. Note that in a purely quantum-mechanical problem, having a real potential, the eigenenergy of such a state would necessarily have a finite imaginary part [32]—our potentials are, however, complex due to the finite imaginary part of the RS wave numbers, though the latter is small for WG modes. Interestingly, it is the complex potential which allows the state energy in the QMA to have zero imaginary part, even though there is a finite probability for the particle to tunnel through the barrier and to escape from the system.

2. Linear permittivity

We choose here a linear profile in the form

$$\varepsilon(r) = 1 + B\theta(R - r)(1 - r/R), \quad (17)$$

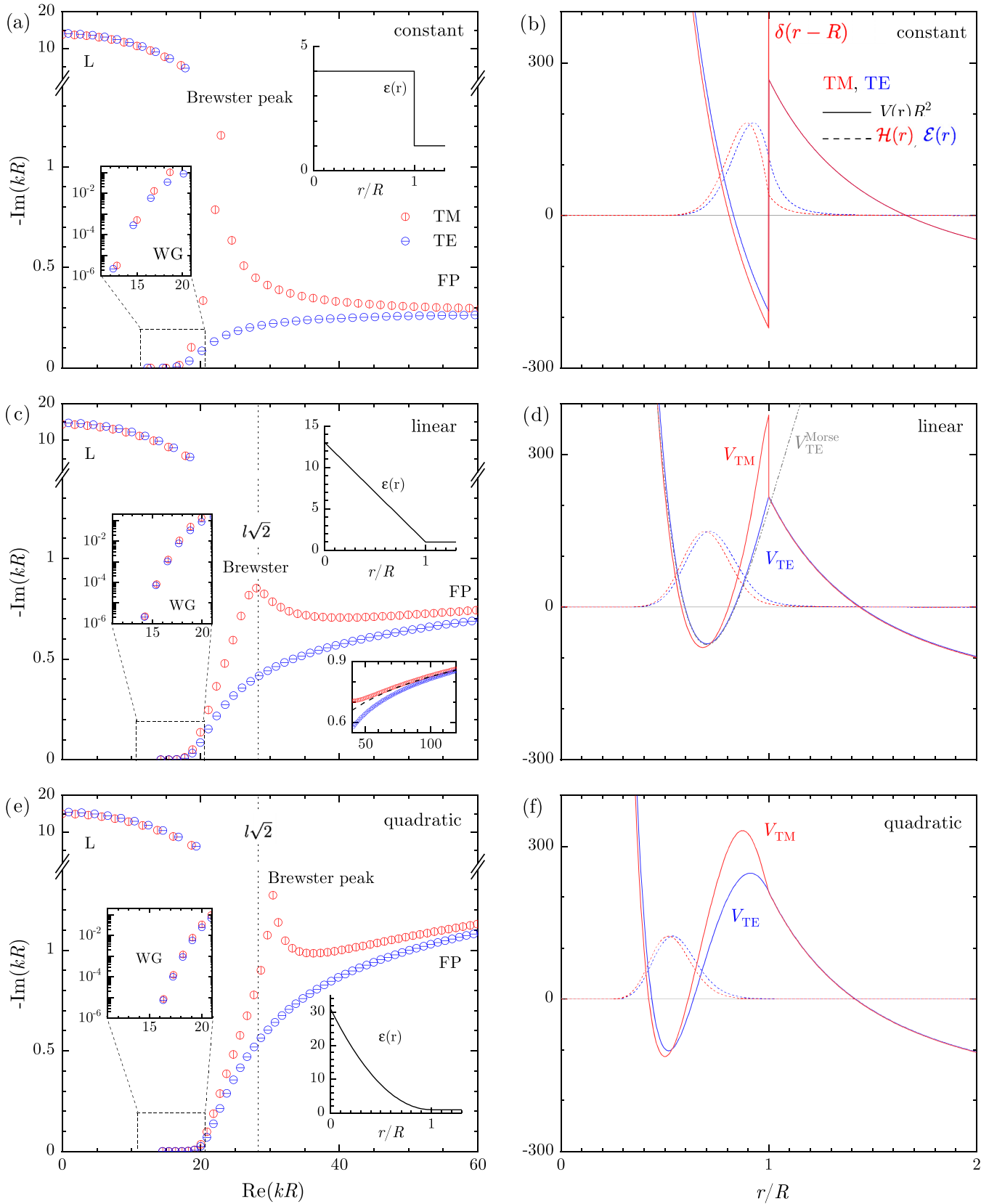


FIG. 3. RSs for $l = 20$, and constant (a), (b); linear (c), (d); and quadratic (e), (f) permittivity profiles as shown in the insets. Left: RSs in the complex k plane. Right: Real part of the potential and the field of the first WG mode. The TE and TM fields are normalized to the same maximum value. The unitless effective potentials $V^{\text{TE}}R^2$ and $V^{\text{TM}}R^2$ are given, respectively, by Eqs. (12) and (14).

so $\varepsilon(r)$ is a continuous function. The parameter B is chosen such that the volume integral of the permittivity $\int \varepsilon(r)dV$ within the sphere of radius R is equal to that of the homogeneous sphere with refractive index n_r , yielding $B = 4(n_r^2 - 1)$. Since the basis system used in the RSE has $n_r = 2$, we take here $B = 12$.

The resulting RS wave numbers calculated via the RSE are shown in Fig. 3(c). Their distribution in the complex k plane is qualitatively similar to that of the homogeneous sphere. The L RSs are nearly unaffected. The WG RSs have a smaller TE-TM splitting and a quicker growth of the imaginary part of k with the real part. The Brewster peak is less pronounced, broader, and is shifted toward larger values of the real part of k . At the sphere boundary, the refractive index is approaching 1, so using Eq. (2) one would expect the Brewster peak to appear at around $k_b R \approx l\sqrt{2}$, which is indeed observed in the spectrum, see dotted line in Fig. 3(c).

The FP RS wave numbers show a significantly larger imaginary part compared the homogeneous case. Also, it is increasing with the real part, which is qualitatively different from the homogeneous sphere, where the imaginary part of k for the FP RSs is converging to a finite value with increasing the real part of k . This can be understood again considering the reflection at the sphere surface. For graded index boundaries, the reflectivity is wavelength dependent. It is proportional to the index change over one wavelength, thus proportional to $1/\text{Re } k$ for short wavelengths. An example of this can be found in Ref. [33] for a segment having an exponential permittivity profile. Using Eq. (3), we therefore expect $\text{Im } k \propto \ln(\text{Re } k)$, which is shown as a dashed line in the lower inset of Fig. 3(c), in good agreement with the high frequency asymptote of TE and TM wave numbers.

To understand the behavior of the WG RSs, we consider the QMA, with potentials shown in Fig. 3(d). The shape of the potentials suggests that they can be approximated with the anharmonic Morse potential [34], for which analytical solutions are known, as detailed in Appendix E. A fit of the Morse potential, matching the zeroth to third derivatives of the potential at its minimum, is shown in Fig. 3(d) for the first WG mode in TE polarization. Using the analytical solutions, we find for the linear permittivity Eq. (17) the following compact expression for the TE WG modes:

$$k_n^{\text{TE}} \approx \frac{\alpha B}{2R(1+B)^{\frac{3}{2}}} \left(3 + \sqrt{3} \frac{2n+1}{\alpha} - 4 \left(\frac{2n+1}{3\alpha} \right)^2 \right)^{\frac{3}{2}}, \quad (18)$$

with the level number $n = 0, 1, \dots$. In this expression, n has the physical meaning of the number of nodes of the field inside the resonator. The accuracy of this expression relies on a high potential barrier, providing a small tunneling (and thus small imaginary part of k) which is typical for WG modes. Therefore, the approximation Eq. (18) has a higher accuracy for the lowest WG modes at higher l and lower n . For $l = 80$, Eq. (18) gives k_n values with a relative error to the RSE values of only 10^{-5} for the first WG mode ($n = 0$), increasing to 10^{-2} for the 12th WG modes ($n = 11$), as illustrated by Table I in Appendix E. Furthermore,

Eq. (18) creates, for $n \ll \alpha$, equidistant levels of spacing $9B/(2R\sqrt{(1+B)^3})$, resembling a harmonic oscillator.

The Morse approximation of the TM potential Eq. (15) for linear permittivity, and of both TE and TM potentials for other spatial dependencies of the permittivity, result in nonlinear simultaneous equations for k_n^2 as detailed in Appendix E. Solving these numerically is still a lower cost compared to using the RSE or solving the radial Eqs. (11) and (13) directly. The Morse approximation also provides analytical wave functions, which can be used for applying perturbation approaches like the one presented in Sec. IV A later.

3. Quadratic permittivity

In addition to the continuity of the permittivity, we can also require that its first derivative is continuous, which can be achieved by using a quadratic profile

$$\varepsilon(r) = 1 + C\theta(R-r)(1-r/R)^2, \quad (19)$$

where we again choose to conserve $\int \varepsilon(r)dV$ relative to the basis system, yielding $C = 10(n_r^2 - 1)$, so $C = 30$ for $n_r = 2$. The resulting RS wave numbers are shown in Fig. 3(e). The RSs change further along the same trends as seen when going from constant to linear profile. Notably, the Brewster peak is shifted further to higher wave numbers compared to constant and linear case. The contrast with the surrounding is lower compared to the linear profile, creating an increased uncertainty in the position of the plane of reflection. It can also be seen from the permittivity profile that the effective radius of the sphere is reduced compared to the constant and linear cases, which results in a larger k_b , in accordance with Eq. (2).

The imaginary part of the FP RSs is increased compared to the linear case as the reflection is further reduced at the surface due to the smooth permittivity. There are still high quality WG modes, with a decreased splitting between TE and TM RSs. Looking at the potential Fig. 3(f), we find the well further inside the sphere with a wide barrier extended toward the outside, which provides good containment for the RSs. Higher-order TM WG modes along with the corresponding TM effective potentials are shown in Fig. 11 of Appendix D.

IV. TE-TM SPLITTING

We found in the previous section that for the linear and quadratic permittivity, the splitting between TE and TM RSs is reduced compared to the constant permittivity, and this effect is further investigated in this section. The degeneracy of TE and TM modes might be of particular interest for chirality sensing, as that can convert second-order perturbation effects due to a chiral material in the surrounding into the first order, similar to the effect of Faraday rotation by a circular magnetic field [35,36]. To understand the cause of the reduced splitting, we first develop in Sec. IV A a perturbative approach. Then, we revisit the optical systems discussed in Sec. III B and quantify the splitting, followed by considering in Sec. IV C a new system featuring a wide effective potential well to reduce the splitting of the fundamental WG mode.

A. Perturbation treatment

The RSs form, together with static modes or their equivalents, a complete set inside the system and therefore provide a suitable basis for expanding any vector field within the system. This is the core principle of the RSE. In fact, an expansion into known basis modes is used in this paper to find the modes of the graded index profiles. In this subsection, we apply the same principle, however, in a simpler situation, namely, we solve the scalar wave equation (13) with the TM potential by expanding its solution into the complete set of eigenstates of the corresponding wave equation (11) for TE polarization. In the simplest case, we reduce our basis to a single TE mode and thus solve Eq. (13) in the so-called diagonal approximation which can further be reduced to and interpreted as a first-order perturbation theory result.

The scalar wave equation (11) for the TE RSs can be written as

$$\hat{L}(k_n, r)\mathcal{E}_n(r) = 0, \quad (20)$$

where

$$\hat{L}(k, r) = \frac{d^2}{dr^2} - \frac{\alpha^2}{r^2} + k^2\varepsilon(r). \quad (21)$$

The corresponding scalar Green's function satisfies

$$\hat{L}(k, r)G_k(r, r') = k\delta(r - r') \quad (22)$$

and can be expanded as

$$G_k(r, r') = \sum_n \frac{\mathcal{E}_n(r)\mathcal{E}_n(r')}{k - k_n} = k \sum_n \frac{\mathcal{E}_n(r)\mathcal{E}_n(r')}{k_n(k - k_n)}, \quad (23)$$

where \mathcal{E}_n is normalized according to Eq. (C3), the same way as in Ref. [21]. Accordingly, Eq. (13) for TM polarization takes the form

$$\hat{L}(k, r)\mathcal{H}(r) = \Delta\hat{L}(r)\mathcal{H}(r), \quad (24)$$

where

$$\Delta\hat{L}(r) = \frac{\varepsilon'(r)}{\varepsilon(r)} \frac{d}{dr}, \quad (25)$$

and can be further written as a Lippmann-Schwinger equation, in terms of the Green's function of the operator $\hat{L}(k, r)$:

$$\mathcal{H}(r) = \frac{1}{k} \int_0^R G_k(r, r') \Delta\hat{L}(r') \mathcal{H}(r') dr'. \quad (26)$$

Now, using the completeness of the basis states $\mathcal{E}_n(r)$,

$$\mathcal{H}(r) = \sum_n c_n \mathcal{E}_n(r), \quad (27)$$

and the Green's function expansion Eq. (23), we convert Eq. (26) into the following matrix equation:

$$k_n(k - k_n)c_n = \sum_{n'} \Delta_{nn'} c_{n'}, \quad (28)$$

where

$$\Delta_{nn'} = \int_0^R \mathcal{E}_n(r) \frac{\varepsilon'}{\varepsilon} \mathcal{E}_{n'}(r) dr \quad (29)$$

and the primes in ε and \mathcal{E} mean derivatives with respect to r . Finally, using a single state only ($n' = n$), this reduces to the

diagonal approximation,

$$k \approx k_n + \frac{\Delta_{nn}}{k_n}, \quad (30)$$

which is clearly equivalent to the first-order result in terms of the perturbation matrix $\Delta_{nn'}$. We call the above method expansion, as the basis functions $\mathcal{E}_n(r)$ used in the expansion Eq. (27) are in turn expanded into the RSs of the homogeneous sphere.

A less rigorous and perhaps simpler approach is to treat the extra term in the TM potential, added to the TE equation, in a single mode approximation, in a manner it is usually applied to closed systems. Assuming $\mathcal{H}(r) \approx \mathcal{E}(r)$ and taking the difference between Eqs. (11) and (13), we find

$$\left[-\frac{\varepsilon'(r)}{\varepsilon(r)} \frac{d}{dr} + (k_{\text{TM}}^2 - k_{\text{TE}}^2)\varepsilon(r) \right] \mathcal{E}(r) \approx 0, \quad (31)$$

where k_{TE} (k_{TM}) is the TE (TM) RS wave number. Multiplying Eq. (31) with $\mathcal{E}(r)$ and integrating over the system volume yields

$$k_{\text{TM}}^2 - k_{\text{TE}}^2 \approx \frac{\int_0^R \mathcal{E}(r) \frac{\varepsilon'(r)}{\varepsilon(r)} \mathcal{E}'(r) dr}{\int_0^R \mathcal{E}(r) \varepsilon(r) \mathcal{E}(r) dr} \equiv 2\Delta. \quad (32)$$

The first-order correction to the wave number, determining the TE-TM splitting, is then given by

$$k_{\text{TM}} \approx k_{\text{TE}} + \frac{\Delta}{k_{\text{TE}}}. \quad (33)$$

For high-quality WG modes, the field $\mathcal{E}(r)$ is small at the surface, so the integral in the denominator of Eq. (32) is getting close to the exact normalization, $2 \int_0^R \varepsilon(r) \mathcal{E}^2(r) dr \approx 1$, and the two results, Eqs. (30) and (33), become identical.

B. Constant, linear and quadratic profiles

The exact splitting of TE and TM RSs is quantified in Fig. 4, showing the distance from each TE RS to its nearest TM RS, both in the complex plane [Fig. 4(a)] and for the real part only [Fig. 4(b)]. Considering first the constant permittivity (black circles), we find that the TE-TM splitting of WG modes is smaller than that of FP modes, and the real part of the splitting changes its sign at the Brewster peak, due to the additional TM mode as discussed in Sec. II A. At this peak, there is a maximum of the absolute difference, due to the much larger imaginary part of the TM mode.

Moving to the linear profile (blue diamonds), the splitting decreases by a factor of about 5 for the WG modes, but only by about 30% for FP modes. Consistent with the weaker Brewster peak in the spectrum [see Fig. 3(c)], the splitting also does not show a pronounced peak. Finally, for the quadratic profile (red squares), the splitting is further reduced by a factor of about 2 for the WG modes and by about 10% for the FP modes. Due to the larger imaginary part [see Fig. 3(e)], also the absolute difference shows a Brewster peak. For all three cases, the smallest absolute distance between RSs is found for the WG modes near the critical wave number $k_c = l/R$ of the total internal reflection.

A similar behavior is observable for higher l , as shown in Appendix F. In this case, it is also easier to see that the graded

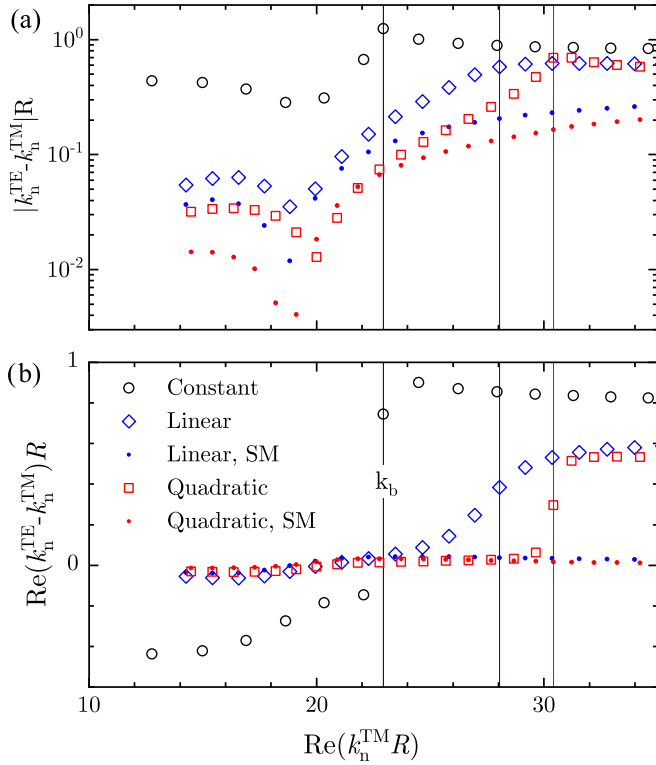


FIG. 4. Absolute value (a) and the real part (b) of the splitting between a TE (k_{TE}) and the nearest TM (k_{TM}) RS, for the considered permittivity profiles and $l = 20$. The vertical lines are the positions of the Brewster peak (k_b) in each TM spectra. The single-mode (SM) values are based on the re-expansion Eq. (30).

permittivity profile reduces the dispersion of the WG modes, creating an approximately equidistant spectrum as shown in Appendix G. This has been also discussed in literature [15] and is consistent with results from the Morse potential approximation given by Eq. (18).

The RS splitting can be understood more mathematically by looking at the additional term of the TM potential in Eq. (14), which is the product of the logarithmic derivatives of the permittivity and the field. An obvious way to reduce the influence of this term is to spatially separate the maxima of the logarithmic derivative of the permittivity and the field amplitude. For the constant permittivity, the derivative creates a δ function at the boundary which overlaps much with the field thus creating a rather large splitting. Moving to the linear profile, the field maximum is shifted to smaller radii but the derivative of the permittivity is constant everywhere within the sphere. Still its influence is more spatially distributed compared to the δ function, and this reduces the splitting. Finally, for the quadratic profile, the maxima of both functions are spatially separated, and this reduces the splitting even further.

We also evaluated the TE-TM mode splitting using the diagonal approximation Eq. (30) for the linear (blue dots) and quadratic (red dots) profiles and compare it with the accurate RSE result in Fig. 4. The obtained values from the single mode approximation are in qualitative but not quantitative agreement with the RSE result, and for the WG modes about a factor of 2 smaller. So, interestingly, while the TE-TM splitting is small, suggesting that a single mode approxima-

tion would be suitable, the TE and TM field distributions are actually significantly different. This is due to a rather large perturbation of the potential (see Fig. 3), showing both positive and negative regions, and thus mixing with other modes while having a small single-mode perturbation integral.

A qualitative discussion of the TE-TM splitting of the fundamental WG mode is provided in Appendix F, in terms of the radial and polar confinement of light in an effective waveguide with an asymmetric cross section.

C. Reduction of splitting in a wide potential well

We expect the TE-TM degeneracy may be reduced for a wider potential well, as this can decrease the overlap of the RS field with the gradients of the permittivity, thus reducing the perturbation of the potential treated in Sec. IV A. To create such a well in the effective potential V^{TE} , given by Eq. (12), the centrifugal radial term α^2/r^2 has to be compensated by a permittivity with the same functional dependence, $\varepsilon(r) \propto 1/r^2$. In this case the refractive index $n(r)$ scales as $1/r$, so the circular round-trip phase, $2\pi k r n(r)$, which is equal to $2\pi l$ in the ray picture, is independent of r . In other words, this graded index creates equal optical ray path lengths at all radii.

Since a permittivity diverging towards the sphere center is not realistic, we introduce a cutoff radius $r_0 \ll R$ at which the permittivity saturates, using the expression

$$\varepsilon_w(r) = \varepsilon_w \frac{R^2 + r_0^2}{r^2 + r_0^2}. \quad (34)$$

Here ε_w is the permittivity at the sphere surface $r = R$. To create a smooth potential with no discontinuities up to the first derivative across the sphere surface, we further introduce a transition region of width r_0 by defining the permittivity as

$$\varepsilon(r) = \begin{cases} 1 & r > R, \\ \varepsilon_w(r) & r < R - r_0, \\ 1 + [\varepsilon_w(r) - 1] \sin^2(\pi \frac{r-R}{2r_0}) & \text{otherwise.} \end{cases} \quad (35)$$

The resulting permittivity profile and RSs for $\varepsilon_w = 2$ and $r_0 = 0.1R$ are shown in Fig. 5(a), calculated by the RSE with $N = 1600$ ($k_{\text{max}} R \approx 1200$). The number of basis modes was increased to retain the accuracy at the higher perturbation strength used. The Brewster peak is blended in with the rest of the TM RSs, which have a monotonously increasing imaginary part; however, we can still identify the peak in the difference of the imaginary part compared to the TE RSs. The potential for the first WG mode [Fig. 5(b)] shows a wide and flat well, as designed. The splitting between TE and TM RSs [see black in Fig. 5(c)] has reduced overall compared to the other profiles considered, and now the smallest absolute distance is observed for the first WG mode, being about twice smaller than for the quadratic profile (see Fig. 4). Increasing r_0 reduces the well width leading to larger splitting [see red in Figs. 5(c) and 5(d)]. When using a sharp boundary at the edge, i.e., without the \sin^2 term in Eq. (35), the splitting of the first mode is not significantly changed, as it has a small field at the boundary. Higher order modes instead acquire a larger splitting, and furthermore a sharper Brewster's peak is found [see blue in Figs. 5(c) and 5(d)].

We also calculated the splitting using the perturbation method introduced in Sec. IV A. While the degeneracy in k is

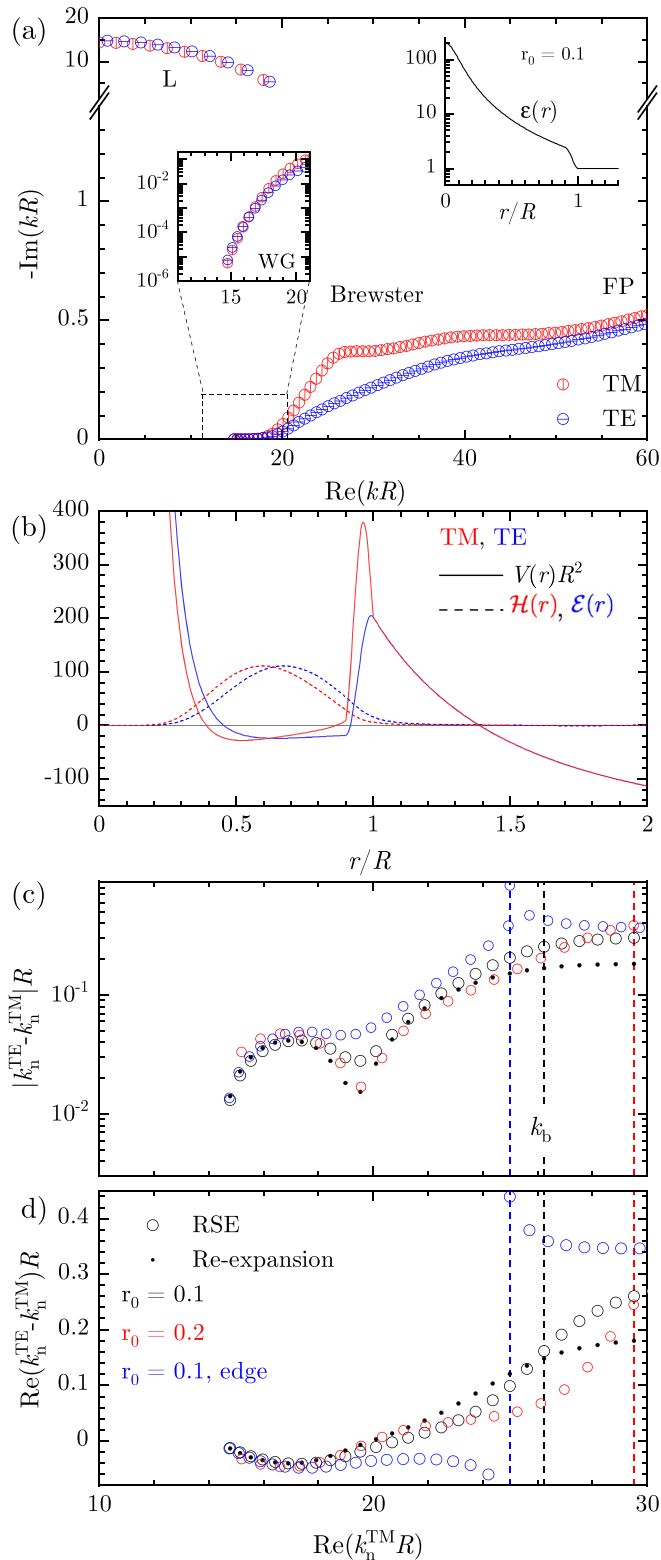


FIG. 5. RSs in a graded index profile Eq. (35) creating a wide potential well. (a) As Fig. 3 left column. (b) As Fig. 3 right column. (c), (d) As Fig. 4 but using Eq. (28) with $N = 100$ basis modes, in comparison with the full RSE. As the imaginary part of k_n is monotonously increasing from WG to FP modes, the Brewster peak value k_b is chosen at the mode that has the largest difference of $\text{Im } k$ between the closest TE and TM modes.

decreased, the TE and TM fields are still spatially separated, so instead of using a single mode we evaluate the full matrix equation Eq. (28) for $N = 100$ RSs. In Fig. 5, we can see that this leads to a much better agreement with the results compared to the single mode approximation used for the linear and quadratic case before. For increasing k the error in the results increases. This is due to a combination of factors, including the truncation of the matrix, the slow convergence of the expansion Eq. (23) as discussed in Ref. [21], and the error in the unperturbed fields \mathcal{E}_n .

V. SUMMARY

We have studied, for different static-mode sets, an optimized version of the RSE and demonstrated the same quick ($1/N^3$, where N is the basis size of the RSE) convergence to the exact solution for different static-mode sets. We have also compared it with a similar version of the RSE, studied earlier in Ref. [21], in which static modes are eliminated from the basis, and demonstrated the same convergence for both versions. We then applied the RSE to spheres with graded permittivity profiles and showed that the RSE is a reliable and simple method to determine all the RSs up to a maximum wave number controlled by the basis choice. Looking at the full spectrum provided by the RSE, instead of just distinct RSs, allows us to identify physical phenomena reliably and rapidly, as shown by the results presented. We have further discussed the results using the ray picture with surface reflections, the phase analysis based on the secular equation, and the concept of an effective potential, treating the radial wave equation as a quantum-mechanical analog. Importantly, we provide a MATLAB program to calculate modes of a spherically symmetric system with a polynomial permittivity profile [37]. Once the basis modes are calculated across the whole system volume, applying the perturbation and finding the new modes takes only a few seconds on a modern computer, therefore the RSE is particularly suited to explore large parameter spaces. From the eigenmodes of graded index spheres one can calculate their scattering cross section [38]. The results shown here are thus relevant for applications such as atmospheric aerosol detection by light detection and ranging [39], the modeling of the human head in medical imaging [40,41], and the propagation of EM waves around earth [42].

For a homogeneous sphere, we have provided a detailed analysis of the spectrum of the RSs in the complex wave-number plane, consisting of leaky, FP, and WG modes. This analysis includes development of a number of approximations. For TM polarization, we have explained the peak in the RS linewidth and an additional mode with respect to TE polarization in terms of the Brewster phenomena. Using the ray picture further, we have evaluated the RS linewidth from Fresnel's coefficients of reflection, which provides a good agreement with the exact solution for FP modes. We have shown that the wave number $k_c = l/R$ evaluated at the critical angle of the total internal reflection plays the role of a boundary in the spectrum separating the WG from FP modes. Using the phase analysis of the secular equation, we developed an analytic approximation for the WG and FP mode

line widths, an asymptotic formula for the FP wave numbers at large frequencies, and have shed light on the mode separation and TE-TM splitting.

We then investigated graded index spheres with linear or quadratic permittivity profiles eliminating the discontinuity at the sphere surface. We found that the imaginary part of FP modes is increasing logarithmically with their wave number, with a larger slope for quadratic profiles. We used the concept of an effective potential for the radial EM wave equation and suggested an interpretation of this quantum-mechanical analogy by associating all the physical solutions with zero-energy states, emphasizing that the effective potentials are complex. This provides a clear picture explaining the existence and properties of WG modes. We further approximated the obtained effective potentials around their minimum with the analytically solvable Morse potential, which for TE polarization yields a simple explicit algebraic expression of high accuracy for the WG mode wave numbers. For large angular quantum numbers l , this solution predicts a nearly equidistant spectrum of WG modes, similar to that of a harmonic oscillator.

We studied the TE-TM splitting and demonstrated its sequential reduction for WG modes when going from constant to linear and then to quadratic permittivity profile. We have shown that the splitting is further reduced in a wide flat potential well designed via the radial permittivity. To understand the TE-TM splitting, we developed a re-expansion method, which perturbatively treats the difference between the effective potentials of TE and TM polarizations. The results are in good agreement with the exact solution. We have also provided a diagonal approximation, which turns out to be insufficient for the investigated cases despite the small splitting—a consequence of the underlying strong perturbation. Using this understanding, we designed a graded index profile providing a wide effective potential well leading to a reduced TE-TM splitting, which in turn enhances the sensitivity of optical systems to chiral materials.

Information on the data created during this research, including how to access it, is available from the Cardiff University data archive [43].

ACKNOWLEDGMENT

Z.S. acknowledges the Engineering and Physical Sciences Research Council for his PhD studentship award (Grant No. EP/R513003/1).

APPENDIX A: PHASE ANALYSIS FOR A SPHERE

The RS wave numbers of a homogeneous sphere in vacuum are determined by the secular equation (1). Its approximate solution Eqs. (8) and (9) developed in Sec. II B is illustrated in Fig. 6. The green solid lines show $\Psi(\text{Re } k) - n\pi$, for all values of n , while blue and red solid lines show the real part of $\Phi(\text{Re } k)$ for TE and TM polarizations, respectively. According to Eq. (8), they should cross the green lines at the real part of the RS wave numbers, $\text{Re } k_n$, whereas the imaginary part Im

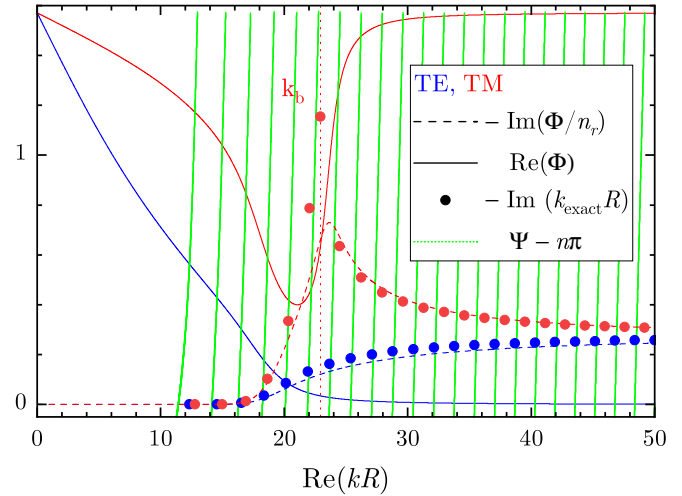


FIG. 6. Phase functions $\Psi(\text{Re } k)$ (green lines), $\text{Re}(\Phi(\text{Re } k))$ (solid lines) and $\text{Im}(\Phi(\text{Re } k))/n_r$ (dashed lines) for TE and TM RSs, alongside the exact RS wave numbers (blue and red dots) in the complex wave-number plane, for a homogeneous sphere of $n_r = 2$ and $l = 20$. The vertical dotted line shows the Brewster wave number k_b .

k_n is approximately given by $\text{Im}(\Phi(\text{Re } k_n))/n_r$ (blue and red dashed lines), according to Eq. (9). Generally, there can be seen a good agreement with the exact values shown by blue and red dots, representing the RS wave numbers in the complex k -plane. At large kR , $\text{Re } \Phi(k)$ approaches the asymptote at 0 ($\pi/2$) for TE (TM) polarization, which determines the mode separation, in accordance with Eq. (10). For a twice larger refractive index of the sphere ($n_r = 4$), and l reduced to 10 in order to create a similar number of WG modes, an improved agreement between this approximation and the exact solution is found, as shown in Fig. 7.

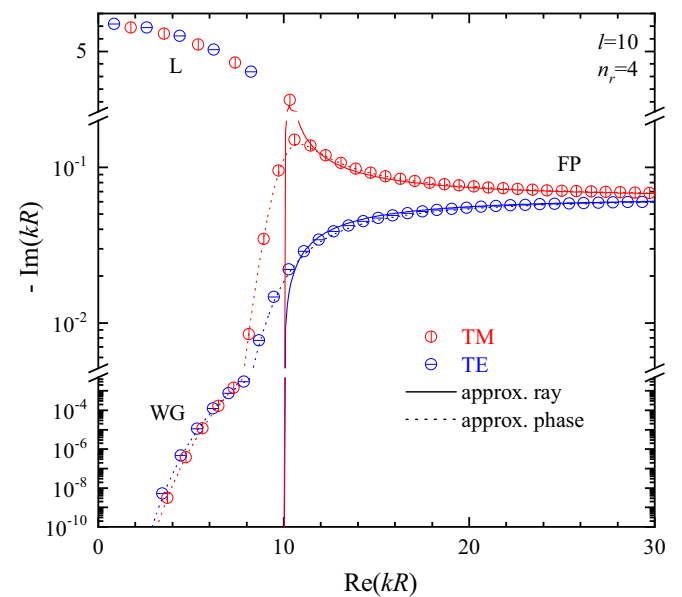


FIG. 7. As Fig. 1 but for $n_r = 4$ and $l = 10$.

To derive the large- k approximation given by Eq. (10), we first note that for $z \gg l$,

$$\frac{H'(z)}{H(z)} \approx i. \quad (\text{A1})$$

Introducing $\tilde{z} = n_r z - (l+1)\pi/2$, where $z = kR$, and also using the approximation Eq. (4), the secular equation (1) takes the form

$$\tan(\tilde{z}) \approx -\frac{i}{\beta}, \quad (\text{A2})$$

which can be also written as

$$e^{2i\tilde{z}} \approx \frac{1+1/\beta}{1-1/\beta}. \quad (\text{A3})$$

This equation has explicit analytical solutions

$$\begin{aligned} \tilde{z}_n^{\text{TE}} &\approx \pi n - \frac{i}{2} \ln \frac{n_r + 1}{n_r - 1}, \\ \tilde{z}_n^{\text{TM}} &\approx \pi \left(n + \frac{1}{2} \right) - \frac{i}{2} \ln \frac{n_r + 1}{n_r - 1}, \end{aligned} \quad (\text{A4})$$

equivalent to Eq. (10). The TE result was also given in Ref. [44]. Note that apart from the $-(l+1)\pi/2$ term in \tilde{z} , these are the same as the modes of a homogeneous slab at normal incidence [17]. The TE (TM) modes correspond to the odd (even) modes of the slab, as discussed in more depth in Appendix B below. From here, we find, in particular, that the wave-number difference between neighboring modes in a given polarization is $\pi/n_r R$, consistent with the graphical solution in Fig. 6. We can also see that the difference between neighboring TE and TM FP RSs is

$$\Delta\tilde{z} = n_r(k^{\text{TM}} - k^{\text{TE}})R = \frac{\pi}{2}, \quad (\text{A5})$$

as also suggested by Fig. 6.

In principle, a similar result can be derived for WG modes in the case when $n_r \gg 1$. The latter condition allows the argument of the Bessel functions ($n_r kR$) to be large (compared to l), leading to the approximation Eq. (4), while simultaneously keeping the argument of the Hankel function small (compared to l). In this case, $H'(z)/H(z) \approx -l/z$, which in the WG limit gives a modified equation compared to Eq. (A2):

$$\tan(\tilde{z}) \approx \frac{l}{\beta z}. \quad (\text{A6})$$

Therefore, it is possible to observe in a very high permittivity material nearly equidistant WG modes even in a homogeneous sphere. This is consistent with Ref. [45], where the resonances positions and mode separations were described based on geometrical optics, and also with approximate results from Ref. [46] for the mode spacing when $l \gg 1$.

APPENDIX B: EIGENMODES OF A HOMOGENEOUS SLAB

By approximating the surface of the sphere with a flat boundary, we compare the modes of a sphere with those of a homogeneous slab, in which EM waves propagate at a non-normal incidence to the boundary. We also compare here the

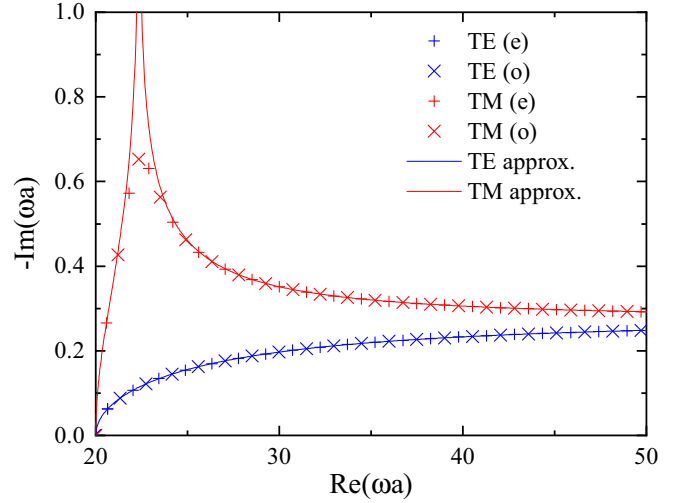


FIG. 8. Eigenmodes of a homogeneous slab with $\epsilon = 4$, $\mu = 1$, and $p = 20$, along with approximate solutions for the imaginary part obtained from Eq. (B2). (e) and (o) label the even and odd modes, respectively. Here ω is the wave number in vacuum.

modes of the slab with an approximation similar to Eq. (3), which is provided by the ray picture.

The secular equation determining the TE modes of a homogeneous slab of thickness $2a$, permittivity ϵ , and permeability μ is given by [47]

$$e^{2iq_n a} = (-1)^n \frac{q_n + \mu k_n}{q_n - \mu k_n}, \quad (\text{B1})$$

where $q = \sqrt{\epsilon\mu\omega^2 - p^2}$ and $k = \sqrt{\omega^2 - p^2}$ are the normal components of wave vector inside the slab and in vacuum, respectively, ω is the length of the wave vector in vacuum, and p is its in-plane component, which is conserved. Note that p was also introduced to discuss the Brewster peak, see Fig. 2. The factor $(-1)^n$ gives the mode parity and can be used to label the modes. The corresponding equation for TM modes is provided by just swapping ϵ and μ in Eq. (B1). We note the similarity between Eqs. (B1) and (A3)—these equations become identical for normal incidence, when $p = 0$ and thus $q = n_r k$ with $n_r = \sqrt{\epsilon\mu}$.

One can find an approximate imaginary part of the mode wave numbers in the same way as described in Sec. II A. The angle of incidence inside the slab is given by $\theta = \text{atan}(p/q)$, and the optical path length is $L = 2an_r/\cos\theta$ where a is the slab half width. The imaginary part of the RS wave numbers is then given by

$$\text{Im } k = \frac{\ln |r_p|}{2an_r} \cos\theta, \quad (\text{B2})$$

where again r_p is the polarization dependent Fresnel coefficient taken at real wave numbers—compare Eqs. (B2) and (3).

We show in Fig. 8 the TE and TM modes of a slab with permittivity $\epsilon = 4$, permeability $\mu = 1$, and in-plane wave number $p = 20/a$, so the system parameters are matching those used for the sphere in Sec. II A. In the TM spectrum, there is a peak again, which is aligned with the position of the Brewster angle. Overall, for these parameters, the approximation works better for the slab than for the sphere, as the

boundary is strictly flat. The observed small deviation of the modes from the approximation at the Brewster peak stems from the neglecting the imaginary part of the wave number in r_p , which can be significant around the peak. We can see that for both polarizations, there are even and odd modes alternating with increasing $\text{Re}(\omega a)$. We can also see that at high frequencies, both TE and TM FP modes converge to the same asymptote, which is the same behavior as for the sphere. As in the spherical case, the TE and TM modes of the same parity appear in alternating order. In fact, even TE modes align with the odd TM modes, and vice versa. However, in case of a sphere even modes do not exist. Finally, instead of the WG modes of a sphere, in case of a slab there are waveguide modes with purely real eigenfrequencies, formed as a consequence of total internal reflection at the planar boundary, and instead of the L modes of a sphere, there are antiwaveguide modes in a slab [48]. Both waveguide and antiwaveguide modes have $\omega < p$ and are not shown in Fig. 8.

APPENDIX C: RESONANT-STATE EXPANSION FOR SPHERICALLY SYMMETRIC SYSTEMS

According to Ref. [21], the matrix equation of the RSE for nondispersive systems has the following general form:

$$(k - k_n)a_n = -k \sum_{n'} \tilde{V}_{nn'} a_{n'}, \quad (\text{C1})$$

where a_n are the expansion coefficients of a perturbed RS into the basis RSs labeled by index n . For spherically symmetric systems, all n refer to the same spherical quantum numbers l and m , but the matrix elements $\tilde{V}_{nn'}$ of the perturbation are quite different in TE and TM polarizations.

For a radially dependent permittivity perturbation $\Delta\varepsilon(r)$ of a nonmagnetic system, the matrix elements in TE polarization are given by

$$\tilde{V}_{nn'}^{\text{TE}} = \int_0^R \mathcal{E}_n(r) \Delta\varepsilon(r) \mathcal{E}_{n'}(r) dr, \quad (\text{C2})$$

where $\mathcal{E}_n(r)$ is the electric field of the basis RS n , satisfying Eq. (11), in which $k = k_n$ is the RS wave number and $\varepsilon(r)$ is the permittivity profile of the basis system, and the boundary condition is that there are only outgoing waves from the system. The fields $\mathcal{E}_n(r)$ are normalized according to [17,21]

$$2 \int_0^R \varepsilon \mathcal{E}_n^2 dr + \frac{1}{k_n} [(\mathcal{E}_n r \mathcal{E}_n')' - 2r(\mathcal{E}_n')^2]_{r=R} = 1. \quad (\text{C3})$$

For TM polarization, the matrix elements have a more complex form:

$$\tilde{V}_{nn'}^{\text{TM}} = V_{nn'} - \sum_{jj'} V_{nj} W_{jj'} V_{j'n'}, \quad (\text{C4})$$

where $W_{jj'}$ is the inverse of matrix $\delta_{jj'} + V_{jj'}$, index n labels the basis TM RSs, and index j labels additional functions required for completeness. They are used in the expansion of the perturbed EM vector fields and the dyadic GF, and are responsible for the static pole representation of the latter [21]. It is convenient to introduce a combined index ν which labels together the RSs (n) and the additional basis functions (j). It is also useful to separate each basis electric vector field into

the radial $\mathcal{E}_\nu^r(r)$ and tangent $\mathcal{E}_\nu^t(r)$ components. The matrix elements contributing to Eq. (C4) then take the form [21]

$$V_{\nu\nu'} = \int_0^R \left[\mathcal{E}_\nu^t \Delta\varepsilon(r) \mathcal{E}_{\nu'}^t + \mathcal{E}_\nu^r \frac{\varepsilon(r) \Delta\varepsilon(r)}{\varepsilon(r) + \Delta\varepsilon(r)} \mathcal{E}_{\nu'}^r \right] dr \quad (\text{C5})$$

with $\mathcal{E}_\nu^t(r)$ and $\mathcal{E}_\nu^r(r)$ defined below.

For the basis TM RSs, the fields are given by

$$\begin{pmatrix} \mathcal{E}_n^t(r) \\ \mathcal{E}_n^r(r) \end{pmatrix} = -\frac{1}{k_n \varepsilon(r)} \begin{pmatrix} \frac{d}{dr} \\ \frac{\varepsilon}{r} \end{pmatrix} \mathcal{H}_n(r) \equiv \begin{pmatrix} \mathcal{K}_n(r) \\ \mathcal{N}_n(r) \end{pmatrix}, \quad (\text{C6})$$

where $\mathcal{H}_n(r)$ is the magnetic field of the basis TM RS n , satisfying Eq. (13), in which $k = k_n$ is the RS wave number and $\varepsilon(r)$ is the permittivity profile of the basis system, with outgoing waves boundary condition. The fields $\mathcal{H}_n(r)$ are normalized according to [17,21]

$$2 \int_0^R \mathcal{H}_n^2 dr + \frac{1}{k_n} \left[\left(\mathcal{H}_n \frac{r}{\varepsilon(r)} \mathcal{H}_n' \right)' - \frac{2r}{\varepsilon(r)} (\mathcal{H}_n')^2 \right]_{r=R_+} = 1 \quad (\text{C7})$$

with $R_+ = R + 0_+$, where 0_+ is a positive infinitesimal.

All other basis states can be expressed in terms of functions $\mathcal{K}_n(r)$ and $\mathcal{N}_n(r)$ introduced in Eq. (C6) and static modes $\psi_\lambda(r)$ introduced in Ref. [20] and also discussed in Ref. [21]. Let us note at this point that the two slightly different versions of the efficient (i.e., quickly convergent) RSE developed in Ref. [21] are based on two different Mittag-Leffler representations of the full dyadic GF of a spherically symmetric system, called in [21] ML3 and ML4. Essentially, they differ in the basis functions describing the static pole of the GF. Also, ML4 is introduced for a homogeneous sphere only, while ML3 is valid for any spherically symmetric basis system.

In the ML3 version of the RSE, all the additional basis states can be divided into three groups. In the first two groups, indices j_{I} and j_{II} take the same values as the TM RS index n , and the fields are given by

$$\begin{pmatrix} \mathcal{E}_{j_{\text{I}}}^t \\ \mathcal{E}_{j_{\text{I}}}^r \end{pmatrix} = \begin{pmatrix} i\mathcal{K}_n \\ i\mathcal{N}_n \end{pmatrix} \quad \text{and} \quad \begin{pmatrix} \mathcal{E}_{j_{\text{II}}}^t \\ \mathcal{E}_{j_{\text{II}}}^r \end{pmatrix} = \begin{pmatrix} \mathcal{K}_n \\ 0 \end{pmatrix}. \quad (\text{C8})$$

In the third group,

$$\begin{pmatrix} \mathcal{E}_{j_{\text{III}}}^t \\ \mathcal{E}_{j_{\text{III}}}^r \end{pmatrix} = \begin{pmatrix} \alpha \psi_\lambda \\ 0 \end{pmatrix}, \quad (\text{C9})$$

and the index j_{III} coincides with λ labeling static modes defined in terms of the radial part of their potential function $\psi_\lambda(r)$. Static modes are the solutions of a generalized Sturm-Liouville problem [20,21] and are normalized according to

$$\lambda^2 \int_0^R \varepsilon(r) \psi_\lambda^2(r) r^2 dr = 1. \quad (\text{C10})$$

For a basis system in the form of a nonmagnetic homogeneous sphere in vacuum, described by the permittivity profile given by

$$\varepsilon(r) = (\varepsilon - 1)\theta(R - r) + 1, \quad (\text{C11})$$

the static mode potentials take the explicit form

$$\psi_\lambda(r) = A_\lambda j_l(\lambda r) \quad (\text{C12})$$

within the sphere ($r \leq R$), where $j_l(x)$ is the spherical Bessel function of order l , λ is the mode eigenvalue (here also used to label the modes), and A_λ is a normalization constant determined according to Eq. (C10). The eigenvalues λ are found from the boundary condition of the Sturm-Liouville problem [20], which leaves a large range of possible sets. Following Ref. [21], we consider here three sets of static modes for the ML3 version of the RSE: (i) the volume-charge set (VC), with the eigenvalues generated by the secular equation

$$\lambda \epsilon R j_l'(\lambda R) + (l+1)j_l(\lambda R) = 0, \quad (\text{C13})$$

(ii) the volume-surface-charge set (VSC), with a simpler secular equation

$$j_l(\lambda R) = 0, \quad (\text{C14})$$

and (iii) a modified-volume-surface-charge set (MVSC), determined by the following secular equation:

$$\lambda R j_l'(\lambda R) + (\epsilon l + 1)j_l(\lambda R) = 0. \quad (\text{C15})$$

Note that apart from the modes generated by the secular equations, both VSC and MVSC sets include one additional mode, that corresponds to $\lambda = 0$. Also note that the VSC and VC sets were used in Ref. [20] for a slowly convergent version of the RSE.

In the ML4 version of the RSE, developed in Ref. [21] for the basis system in a form of a homogeneous sphere in vacuum, all basis states responsible for the static pole of the GF can be divided into four groups. The first two groups are the same as in ML3 and are given by Eq. (C8). The third and fourth groups of basis functions provide an alternative to the static mode sets described above. The third group is given by

$$\begin{pmatrix} \mathcal{E}_{j_{\text{III}}}^t(r) \\ \mathcal{E}_{j_{\text{III}}}^r(r) \end{pmatrix} = \begin{pmatrix} \mathcal{N}_n(r) \\ 0 \end{pmatrix}, \quad (\text{C16})$$

where index j_{III} again takes the same values as the TM RS index n , in the same way as in the first two groups, and the fourth group consists of the single element

$$\begin{pmatrix} \mathcal{E}_{j_{\text{IV}}}^t(r) \\ \mathcal{E}_{j_{\text{IV}}}^r(r) \end{pmatrix} = \begin{pmatrix} \mathcal{M}_0(r) \\ 0 \end{pmatrix}, \quad (\text{C17})$$

where

$$\mathcal{M}_0(r) = \sqrt{\frac{l(l+1)}{\epsilon R} \frac{\epsilon - 1}{\epsilon l + l + 1}} \left(\frac{r}{R}\right)^l, \quad (\text{C18})$$

which can also be found as

$$\begin{aligned} \mathcal{M}_0(r) &= (\epsilon - 1) \sqrt{\frac{l}{\epsilon}} \lim_{k_n \rightarrow 0} \mathcal{K}_n(r) \\ &= (\epsilon - 1) \sqrt{\frac{l+1}{\epsilon}} \lim_{k_n \rightarrow 0} \mathcal{N}_n(r) \end{aligned} \quad (\text{C19})$$

by treating both $\mathcal{K}_n(r)$ and $\mathcal{N}_n(r)$ as analytic functions of k_n and taking the limit $k_n \rightarrow 0$.

To test the convergence of the RSE based on ML3 for the different static mode sets, we apply the RSE to a size perturbation of a homogeneous sphere. We choose as unperturbed system a homogeneous sphere in vacuum, having radius R ,

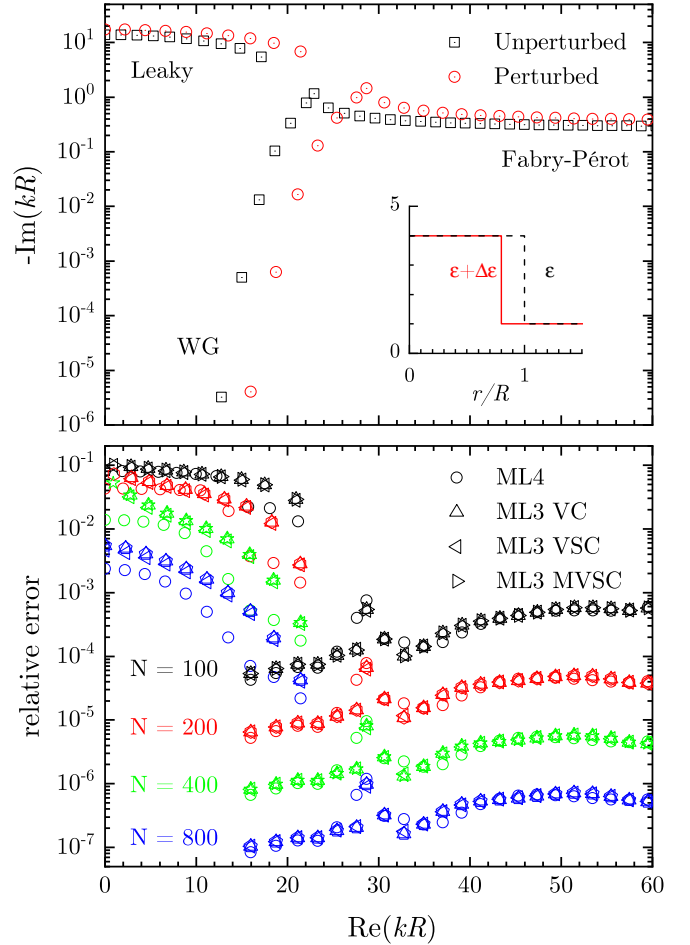


FIG. 9. RSE applied for size perturbation. TM RSs of a dielectric sphere with permittivity $\epsilon = 4$ and permeability $\mu = 1$, for angular momentum number $l = 20$. Top: Wave numbers in the complex k plane. Basis RSs for size R , target RSs for size $0.8R$. Bottom: Relative error of the RSs calculated by the RSE with elimination of static modes (ML4) and with efficient inclusion of static modes (ML3) for various static mode sets and basis sizes N as given. Inset: Unperturbed and perturbed permittivity profiles.

permittivity $\epsilon = 4$, and permeability $\mu = 1$. We focus here on the TM RSs with angular momentum $l = 20$, also noting that in spherically symmetric systems, all states are degenerate in m . The target system is a sphere of the same material and radius $0.8R$, so the perturbation is given by $\Delta\epsilon = 1 - \epsilon$ in the outer $0.2R$ thick shell of the basis sphere. Figure 9 shows the resulting perturbed and unperturbed eigenvalues k , and their error, for various basis sizes N , which include RSs with $|k_n|R \lesssim 0.77N$ and static modes with $|k_\lambda|R \lesssim 3.31N$. For a homogeneous sphere, in the absence of dispersion the RS wave numbers k_n and the sphere radius are inversely proportional, which can be seen as a scaling of the target RSs compared to the basis RSs in the complex plane.

The relative error for ML3 scales as $1/N^3$ (the same as in ML4), independent of which static mode set is used. In the original version of the RSE [20], with a slow ($1/N$) convergence for static mode inclusion, there was a more significant difference between the VC and VSC sets, as

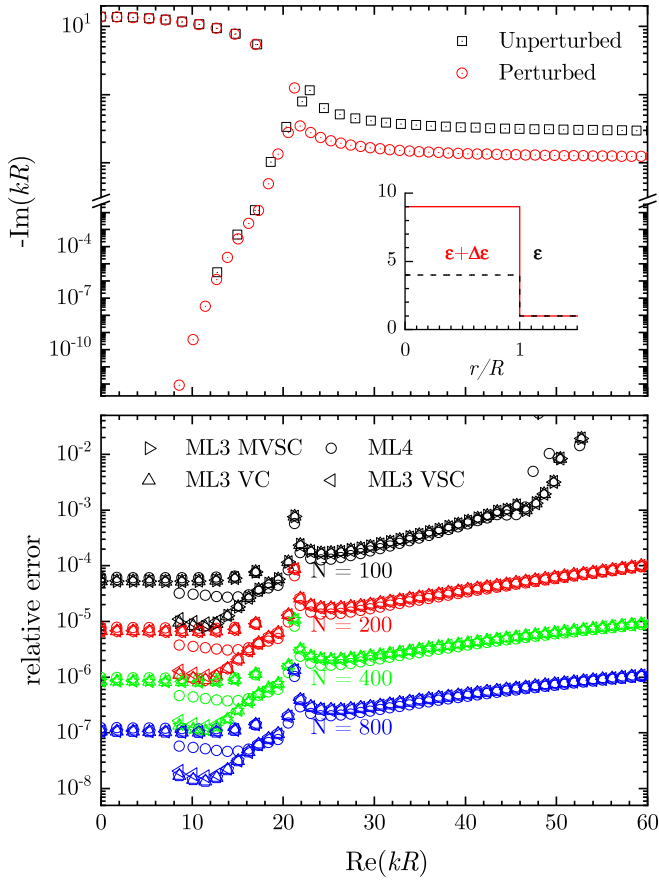


FIG. 10. As Fig. 9, but for a homogeneous perturbation. Basis system $\epsilon = 4$, target system $\epsilon + \Delta\epsilon = 9$.

they were used for the expansion of the complete residue of the static pole of the GF, including the δ function term. We find that ML4 provides smaller errors for the leaky branch. This can be understood by noting that ML4 uses instead of static modes basis functions proportional to the RSs, including L RSs, and thus can be expected to be better suited for expanding the L RSs of the target system. A slow initial convergence of L RSs is testament to their unusual spatial shape, not well described by the basis RSs, but the $1/N^3$ convergence is eventually recovered above $N = 400$.

The results for strength perturbation, that is, changing the permittivity of the sphere homogeneously, are shown in Fig. 10, displaying a similar behavior. Here, using the same basis sizes as in Fig. 9, we apply the RSE for a homogeneous increase of the permittivity of the sphere by $\Delta\epsilon = 5$, giving a target sphere permittivity $\epsilon + \Delta\epsilon = 9$. The higher refractive index leads to a denser array of RSs, increased number of WG modes, and smaller imaginary part for the FP modes. We can see that the error converges with the basis size N as $1/N^3$ for ML3, independent of the static mode set used. For the WG modes, the ML3 representation has some advantage over ML4, having up to five times smaller errors. The static modes thus seem better suited to describe these WG modes, likely because they are bound to the sphere, similar to the WG modes.

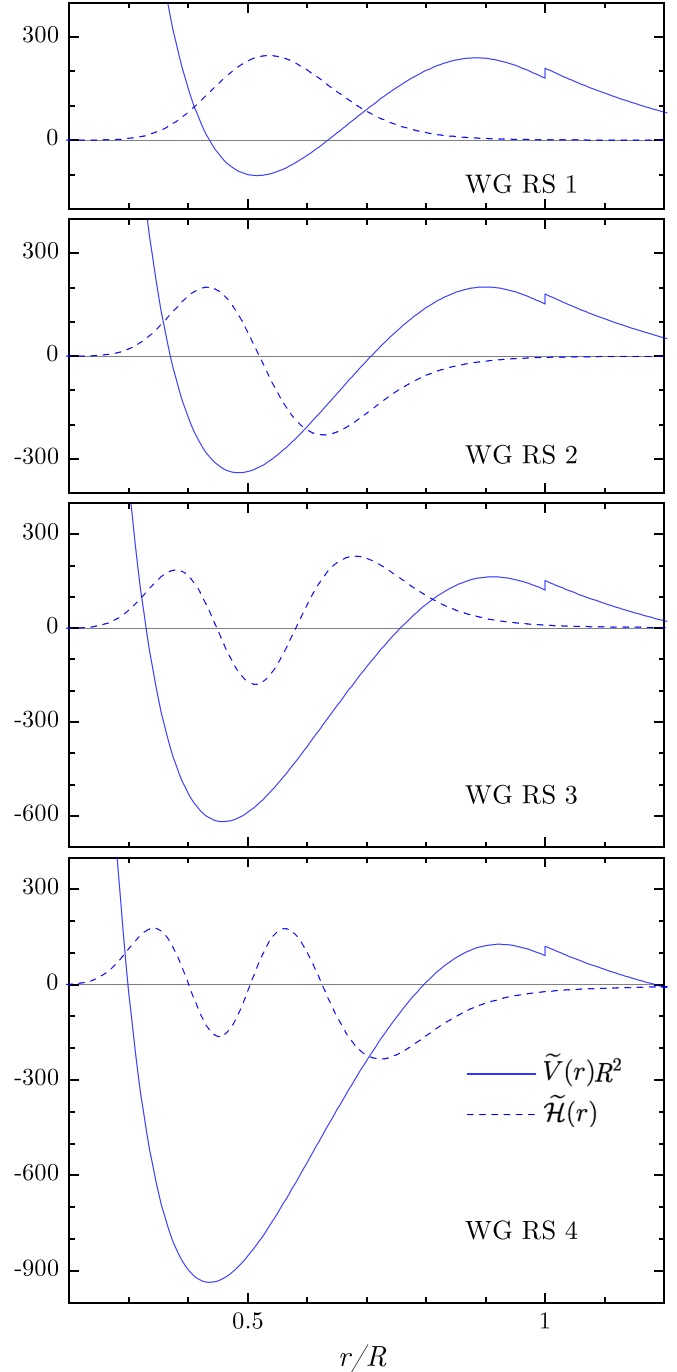


FIG. 11. Real part of the unitless effective potential $\tilde{V}^{\text{TM}}R^2$ and the normalized field $\tilde{\mathcal{H}}$ for the first four TM WG RSs, for the quadratic permittivity profile, and $l = 20$ as in Fig. 3. WG RS 1 $kR = 14.4 - 6.74 \times 10^{-9}i$, WG RS 2 $kR = 15.4 - 3.51 \times 10^{-7}i$, WG RS 3 $kR = 16.3 - 8.47 \times 10^{-6}i$, WG RS 4 $kR = 17.2 - 1.22 \times 10^{-4}i$.

We thus conclude that for all three static mode sets, ML3 has a convergence similar to ML4. We used the ML4 version of the RSE for generating the results of this paper.

APPENDIX D: EFFECTIVE POTENTIAL FOR TM MODES

Here we show that the wave equation (13) for the scalar magnetic field $\mathcal{H}(r)$ in TM polarization can be brought to

a Schrödinger-like equation with an effective potential independent of the wave function. Following Ref. [10], we introduce a substitution $\mathcal{H}(r) = \sqrt{\varepsilon(r)}\tilde{\mathcal{H}}(r)$, from which we find

$$\frac{d\mathcal{H}}{dr} = \frac{1}{2} \frac{\varepsilon'}{\sqrt{\varepsilon}} \tilde{\mathcal{H}} + \sqrt{\varepsilon} \tilde{\mathcal{H}}' \quad (\text{D1})$$

$$\frac{d^2\mathcal{H}}{dr^2} = \left(-\frac{1}{4} \frac{(\varepsilon')^2}{\varepsilon^{\frac{3}{2}}} + \frac{1}{2} \frac{\varepsilon''}{\sqrt{\varepsilon}} \right) \tilde{\mathcal{H}} + \frac{\varepsilon'}{\sqrt{\varepsilon}} \tilde{\mathcal{H}}' + \sqrt{\varepsilon} \tilde{\mathcal{H}}'', \quad (\text{D2})$$

where the prime indicates the derivative with respect to r and where we omit the dependencies on r for brevity. Using these expressions the wave equation takes the form

$$\left(\frac{d^2}{dr^2} - \frac{\alpha^2}{r^2} + k^2\varepsilon - \frac{3}{4} \left(\frac{\varepsilon'}{\varepsilon} \right)^2 + \frac{1}{2} \frac{\varepsilon''}{\varepsilon} \right) \tilde{\mathcal{H}} = 0, \quad (\text{D3})$$

in which the first derivative of the wave function present in Eq. (13) has canceled out, so the corresponding effective potential \tilde{V}^{TM} given by Eq. (15) is independent of the wave function $\tilde{\mathcal{H}}$. This comes at the cost of adding a term containing the second derivative of the permittivity to \tilde{V}^{TM} . We show \tilde{V}^{TM} in Fig. 11 for the lowest four WG modes, for the quadratic permittivity profile described in Sec. III B 3. Overall, the potential has a shape similar to V^{TE} shown in Fig. 3(f), apart from the step at the sphere surface due to the contribution from the second derivative of the permittivity which has a discontinuity. As in the TE polarization, the potential is getting deeper with the mode number, and its minimum is slightly shifting towards the center, as it is clear from Fig. 11.

APPENDIX E: MORSE POTENTIAL

The Morse potential is a nonparabolic potential with known analytical solutions for energy levels and corresponding wave functions, often used to describe the binding of diatomic molecules [49]. We take the Morse potential in the form

$$V_{\text{M}}(r) = D_e \{1 - \exp[-a(r - r_e)]\}^2, \quad (\text{E1})$$

where D_e is the dissociation energy, r_e is the position of the potential minimum, and a is an inverse well width. The potential is zero at $r = r_e$ and approaches D_e asymptotically with increasing r . The bound energy levels of a quantum particle with a mass $M = \hbar^2/2$ in this potential are $E_n = -a^2(\lambda - n - 1/2)^2 + D_e$, where $\lambda = \sqrt{D_e}/a$ and $n = 0, 1, \dots$ with $n < \lambda - 1/2$.

We apply this potential here to find approximate solutions for WG modes in the QMA, given by Eq. (11) for TE and Eq. (D3) for TM polarization. To do so, we match the coefficients of the Taylor expansion of the Morse potential $V_{\text{M}}(r)$ and the corresponding QMA potential $V(r)$ at their minimum r_e up to third order. Matching the value at the minimum is achieved by adding the value $V(r_e)$ to the Morse potential and its eigenenergies:

$$E_n = -a^2(\lambda - n - 1/2)^2 + D_e + V(r_e). \quad (\text{E2})$$

The first derivative of both potentials is zero at the minimum and thus is matched by construction. We then determine D_e

and a by matching the second and third derivatives, yielding

$$V''(r_e) = 2a^2 D_e \quad \text{and} \quad V'''(r_e) = -6a^3 D_e, \quad (\text{E3})$$

where the prime denotes the derivative with respect to r . As $V(r)$ depends on k , each WG mode has its own Morse potential parameters.

Now, since the solution corresponding to the WG mode has zero energy in the QMA, we can find an explicit equation determining the approximate value of the WG mode wave number k_{M} . Eliminating D_e and a from Eqs. (E2) and (E3), and requiring that $E_n = 0$ yields

$$\left[\frac{V'''}{3V''} \left(n + \frac{1}{2} \right) \right]^2 = V + \sqrt{2V''} \left(n + \frac{1}{2} \right), \quad (\text{E4})$$

which is evaluated at $r = r_e$, where r_e is determined by

$$V'(r_e) = 0 \quad \text{with} \quad V''(r_e) > 0, \quad (\text{E5})$$

to select a minimum. Generally, Eqs. (E4) and (E5) provide a nonlinear set of equations for k_{M}^2 , which can be solved numerically. Notably, for the case of a linear permittivity profile $\varepsilon(r)$ and TE polarization, the second and third derivatives of the potential are independent of k . They are given by $V''(r) = 6\alpha^2 R^2/r^4$ and $V'''(r) = -24\alpha^2 R^2/r^5$, so the minimum position is determined by $r_e^3 = -2R\alpha^2/(k^2\varepsilon')$. Inserting these into Eq. (E4) provides the explicit algebraic expression Eq. (18) for the approximate wave numbers of the WG modes. A fit of the effective potential $V(r)$ for the first WG mode ($n = 0$) in TE polarization with a Morse potential $V_{\text{M}}(r)$ is illustrated in Fig. 3(d), showing an excellent visual agreement between the two. Table I shows a comparison of the WG mode wave numbers calculated using the RSE with the approximate ones using the Morse potential, Eq. (18), revealing a high accuracy of the approximation with relative errors in the $10^{-5} - 10^{-3}$ range.

Finally, Table II shows the six lowest states in each of the Morse potentials corresponding to the first five WG modes in TE polarization. The state describing the WG mode has zero energy, and is changing from the first ($n = 0$) to the fifth state

TABLE I. Comparison of TE WG mode wave numbers calculated by the RSE (real part) and the Morse approximation Eq. (18), along with the Morse parameters for each fit. The relative error is calculated with respect to the RSE. Results are shown for the linear permittivity profile as in Sec. III B 2 and $l = 80$.

n	$k_{\text{RSE}R}$	$k_{\text{M}R}$	Relative error	r_e/R	$1/aR$	$D_e R^2$
0	54.11860	54.12054	0.00004	0.71708	0.53781	21266
1	55.26400	55.27396	0.00018	0.70707	0.53030	21872
2	56.40250	56.42867	0.00046	0.69739	0.52304	22484
3	57.53360	57.58464	0.00089	0.68802	0.51602	23100
4	58.65710	58.74180	0.00144	0.67896	0.50922	23721
5	59.77250	59.90012	0.00214	0.67018	0.50263	24347
6	60.87960	61.05955	0.00296	0.66167	0.49625	24977
7	61.97800	62.22004	0.00391	0.65341	0.49006	25612
8	63.06740	63.38155	0.00498	0.64541	0.48405	26251
9	64.14750	64.54401	0.00618	0.63763	0.47822	26895
10	65.21800	65.70736	0.00750	0.63008	0.47256	27544
11	66.27870	66.87152	0.00894	0.62275	0.46706	28196

TABLE II. Energy levels in the five different Morse potentials corresponding to the first five WG modes for TE polarization, $l = 80$, and a linear permittivity profile as in Sec. III B 2.

$k_M R$	WG 1	WG 2	WG 3	WG 4	WG 5
	54.12	55.26	56.40	57.53	58.66
n	$E_n(k_M)R^2$				
0	0	-551	-1124	-1720	-2338
1	535	0	-558	-1139	-1742
2	1064	543	0	-566	-1154
3	1585	1080	551	0	-573
4	2100	1609	1095	558	0
5	2608	2131	1631	1109	565

($n = 4$) in the Morse potential. Importantly, the other states at nonzero energy are not describing WG modes, different from what could be implied by the QMA.

APPENDIX F: QUALITATIVE DISCUSSION OF THE TE-TM SPLITTING AND AN EXAMPLE FOR $l = 80$

One way to understand qualitatively the splitting of the fundamental WG (FWG) mode for a given l is to consider the RSs as light guided around the sphere as in a waveguide with an asymmetric cross section in radial and polar directions. TE RSs have only the tangent component of the electric field, while for TM RSs there is also a radial component. All modes have polar and radial confinement, both due to the spherical geometry. The radial confinement is determined by the effective potential as discussed in detail in Sec. III. As for the polar confinement, it is described, e.g., for the FWG mode with $m = l$ by the analytic dependence of the field which is proportional to $\sin^l(\theta)$, where θ is the polar angle. We can find the angular width Θ of the polar confinement from the half maximum of the intensity $\cos^{2l}(\Theta) = 1/2$, after substituting $\theta = \Theta + \pi/2$ into the above angular dependence of the field. This condition yields $\Theta = \pm\sqrt{\ln(2)}/l$ for $l \gg 1$. The full width at half maximum (FWHM) of the field extension in polar direction w_θ is then approximately given by $w_\theta = 2r_p\sqrt{\ln 2}/l$, with the peak radius r_p of the RS, which for $l = 20$ amounts to about $0.37 r_p$. For the constant permittivity [Fig. 3(b)], we find $r_p \approx 0.9 R$, so $w_\theta \approx 0.33R$ and the FWHM in radial direction $w_r \approx 0.15R$. The RS asymmetry is thus about a factor of 2.2. For the linear permittivity [Fig. 3(d)], we find $r_p \approx 0.71 R$, so $w_\theta \approx 0.26R$ and the FWHM in radial direction $w_r \approx 0.20R$. The FWG mode asymmetry is thus about a factor of 1.3. For the quadratic permittivity [Fig. 3(f)], we find $r_p \approx 0.54 R$, so $w_\theta \approx 0.20R$ and the FWHM in radial direction $w_r \approx 0.17R$. The FWG mode asymmetry is thus about a factor of 1.2. We see from these estimates that the RS asymmetry reduces when going from the constant to the linear and then further to the quadratic profile, and so does the TE-TM splitting.

To reduce the FWG mode asymmetry further, we have designed an index profile demonstrated and discussed in Sec. IV C. Looking at the FWG mode asymmetry in this case, we find $r_p \approx 0.67 R$, so $w_\theta \approx 0.25R$ and the FWHM in radial direction $w_r \approx 0.33R$. The RS asymmetry is thus about a factor of 0.75, inverted compared to the other profiles. Still,

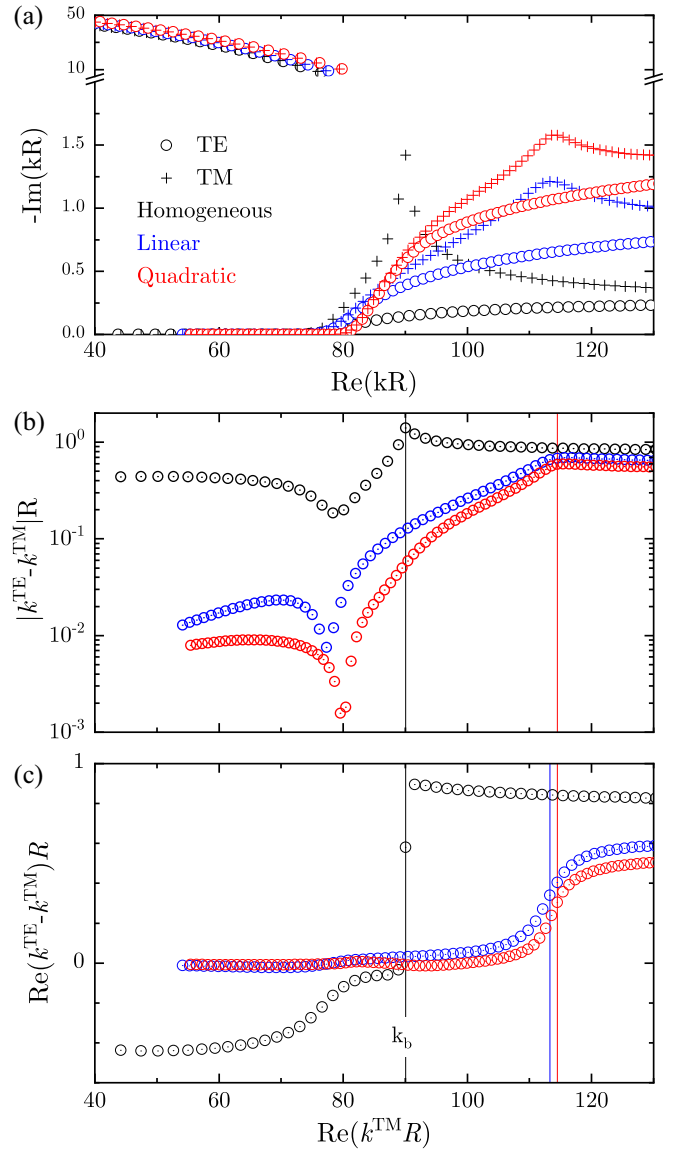


FIG. 12. As Fig. 4, but for $l = 80$.

the splitting has the same sign, showing that the FWG mode asymmetry is not a reliable predictor of the splitting. We note that as the field is extended in the radial direction the curvature of the sphere could be non-negligible, which is not taken into account in the asymmetry analysis.

In Fig. 12, the difference between the TE and nearest TM RSs for $l = 80$ is shown, for the constant, linear, and quadratic permittivity profiles, using a basis size of $N = 800$. The qualitative behavior is similar to $l = 20$ shown in Fig. 4, but the RSs are shifted to higher wave numbers, and more WG RSs are present. For the linear and quadratic profiles the minimum splitting is reduced by approximately a factor of 4. This is consistent with the modes being more tightly packed which can be seen by comparing Fig. 3 and Fig. 12.

APPENDIX G: RS SEPARATION

It is interesting to investigate the RS separation of each polarization for the different permittivity profiles, as shown in Fig. 13. Let us consider in the ray picture a nearly normal

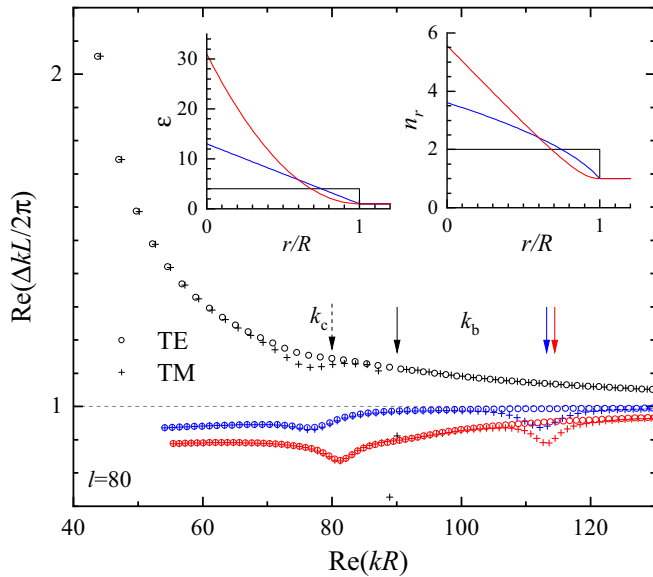


FIG. 13. RS separation for $l = 80$, for constant (black), linear (blue), and quadratic (red) permittivity profiles shown in the left inset. The right inset shows the corresponding refractive index profiles. The separation Δk is taken between a RS at k and the following RS of the same polarization. The vertical arrows indicate positions k_b of the Brewster peak mode and the wave number k_c at the critical angle of total internal reflection.

incidence, corresponding to RS wave numbers much larger than the critical wave number, $k_c = l/R$. In this case, the mode separation Δk can be evaluated from the optical path length between successive reflections, $L = 2 \int_0^R \sqrt{\varepsilon(r)} dr$. L/R takes the values of 4.0, 5.1, and 6.0, for the employed constant, linear, and quadratic permittivity profiles, respectively. Using the resonator condition of constructive interference of waves, $2L = n\lambda_n$, where n is a natural number, and the missing even states discussed in Sec. II B, we find $\Delta k = 2\pi/\lambda_{n+1} - 2\pi/\lambda_n = 2\pi/L$. Therefore, Δk in units of $2\pi/L$ tends toward unity for large k , which can be observed in Fig. 13.

Overall, for the constant profile, the spacing reduces with $\text{Re } k$, while for the linear and quadratic profiles, the spacing is nearly constant, increasing only slightly. There are two regions of deviation from the monotonous behavior, indicated by vertical arrows in Fig. 13. First, at the Brewster peak k_b , where the spacings of TM RSs, which otherwise are nearly identical to the TE RSs, are reduced to accommodate the additional Brewster RS, as discussed in Sec. II A. Second, at the wave number for the critical angle of total internal reflection at the surface, $k_c = l/R$, which is the transition region between WG and FP modes, where both TE and TM RSs show a slightly reduced splitting, somewhat more pronounced for the TM RSs, specifically for the constant permittivity.

- [1] W. Liu, A. E. Miroshnichenko, D. N. Neshev, and Y. S. Kivshar, Broadband unidirectional scattering by magneto-electric core-shell nanoparticles, *ACS Nano* **6**, 5489 (2012).
- [2] P. J. Wyatt, Scattering of electromagnetic plane waves from inhomogeneous spherically symmetric objects, *Phys. Rev.* **127**, 1837 (1962).
- [3] D. Q. Chowdhury, S. C. Hill, and P. W. Barber, Morphology-dependent resonances in radially inhomogeneous spheres, *J. Opt. Soc. Am. A* **8**, 1702 (1991).
- [4] J. P. Huang, K. W. Yu, G. Q. Gu, and M. Karttunen, Electrorotation in graded colloidal suspensions, *Phys. Rev. E* **67**, 051405 (2003).
- [5] A. Shalashov and E. Gospodchikov, Simple approach to electromagnetic scattering by small radially inhomogeneous spheres, *IEEE Trans. Antennas Propag.* **64**, 3960 (2016).
- [6] J. B. Pendry, D. Schurig, and D. R. Smith, Controlling electromagnetic fields, *Science* **312**, 1780 (2006).
- [7] L. W. Casperson, Electromagnetic modes of an inhomogeneous sphere, *J. Opt. Soc. Am.* **65**, 399 (1975).
- [8] J. R. Wait, Electromagnetic scattering from a radially inhomogeneous sphere, *Appl. Sci. Res.* **10**, 441 (1962).
- [9] L. Kai and P. Massoli, Scattering of electromagnetic-plane waves by radially inhomogeneous spheres: A finely stratified sphere model, *Appl. Opt.* **33**, 501 (1994).
- [10] J. A. Lock, Electromagnetic scattering of a plane wave by a radially inhomogeneous sphere in the short wavelength limit, *J. Quant. Spectrosc. Radiat. Transfer* **202**, 126 (2017).
- [11] F. A. Albini, Scattering of a plane wave by an inhomogeneous sphere under the Born approximation, *J. Appl. Phys.* **33**, 3032 (1962).
- [12] L. Dong, G. Q. Gu, and K. W. Yu, First-principles approach to dielectric response of graded spherical particles, *Phys. Rev. B* **67**, 224205 (2003).
- [13] H. M. Lai, P. T. Leung, K. Young, P. W. Barber, and S. C. Hill, Time-independent perturbation for leaking electromagnetic modes in open systems with application to resonances in microdroplets, *Phys. Rev. A* **41**, 5187 (1990).
- [14] P. T. Leung and K. M. Pang, Completeness and time-independent perturbation of morphology-dependent resonances in dielectric spheres, *J. Opt. Soc. Am. B* **13**, 805 (1996).
- [15] V. S. Ilchenko, A. A. Savchenkov, A. B. Matsko, and L. Maleki, Dispersion compensation in whispering-gallery modes, *J. Opt. Soc. Am. A* **20**, 157 (2003).
- [16] V. Laquerbe, R. Pascaud, T. Callegari, L. Liard, and O. Pascal, Analytical model to study the electrostatic resonance of sub-wavelength radially inhomogeneous negative permittivity spheres, *IEEE Antennas Wireless Propag. Lett.* **16**, 2894 (2017).
- [17] E. A. Muljarov, W. Langbein, and R. Zimmermann, Brillouin-Wigner perturbation theory in open electromagnetic systems, *Europhys. Lett.* **92**, 50010 (2010).
- [18] E. A. Muljarov and T. Weiss, Resonant-state expansion for open optical systems: Generalization to magnetic, chiral, and bi-anisotropic materials, *Opt. Lett.* **43**, 1978 (2018).

- [19] M. B. Doost, W. Langbein, and E. A. Muljarov, Resonant-state expansion applied to three-dimensional open optical systems, *Phys. Rev. A* **90**, 013834 (2014).
- [20] S. V. Lobanov, W. Langbein, and E. A. Muljarov, Resonant-state expansion applied to three-dimensional open optical systems: Complete set of static modes, *Phys. Rev. A* **100**, 063811 (2019).
- [21] E. A. Muljarov, Full electromagnetic Green's dyadic of spherically symmetric open optical systems and elimination of static modes from the resonant-state expansion, *Phys. Rev. A* **101**, 053854 (2020).
- [22] L. W. Casperson, Electromagnetic modes of an inhomogeneous sphere, *Appl. Opt.* **20**, 2738 (1981).
- [23] D. W. Vernooy, V. S. Ilchenko, H. Mabuchi, E. W. Streed, and H. J. Kimble, High- Q measurements of fused-silica microspheres in the near infrared, *Opt. Lett.* **23**, 247 (1998).
- [24] A. Perot and C. Fabry, On the application of interference phenomena to the solution of various problems of spectroscopy and metrology, *Astrophys. J.* **9**, 87 (1899).
- [25] D. J. Griffiths, *Introduction to Electrodynamics*, 4th ed. (Cambridge University Press, Cambridge, UK, 2017).
- [26] H. S. Sehmi, W. Langbein, and E. A. Muljarov, Applying the resonant-state expansion to realistic materials with frequency dispersion, *Phys. Rev. B* **101**, 045304 (2020).
- [27] C. C. Lam, P. T. Leung, and K. Young, Explicit asymptotic formulas for the positions, widths, and strengths of resonances in Mie scattering, *J. Opt. Soc. Am. B* **9**, 1585 (1992).
- [28] M. K. Hedayati and M. Elbahri, Antireflective coatings: Conventional stacking layers and ultrathin plasmonic metasurfaces, a mini-review, *Materials* **9**, 497 (2016).
- [29] P. Y. Chen, Y. Sivan, and E. A. Muljarov, An efficient solver for the generalized normal modes of non-uniform open optical resonators, *J. Comput. Phys.* **422**, 109754 (2020).
- [30] B. R. Johnson, Theory of morphology-dependent resonances: Shape resonances and width formulas, *J. Opt. Soc. Am. A* **10**, 343 (1993).
- [31] F. Vollmer and D. Yu, *Optical Whispering Gallery Modes for Biosensing: From Physical Principles to Applications*, 1st ed. (Springer, Cham, Switzerland, 2020).
- [32] A. Baz', Y. Zel'dovich, and A. Perelomov, *Scattering, Reactions and Decay in Nonrelativistic Quantum Mechanics* (U.S. Department of Commerce, Washington, DC, 1969).
- [33] P. Yeh, *Optical Waves in Layered Media*, 1st ed. (Wiley-Interscience, Hoboken, New Jersey, 2005).
- [34] P. M. Morse, Diatomic molecules according to the wave mechanics. II. Vibrational levels, *Phys. Rev.* **34**, 57 (1929).
- [35] S. Lan and M. Hossein-Zadeh, Faraday effect in high- Q whispering-gallery mode optical cavities, *IEEE Photon. J.* **3**, 872 (2011).
- [36] S. Vincent, X. Jiang, P. Russell, and F. Vollmer, Thermally tunable whispering-gallery mode cavities for magneto-optics, *Appl. Phys. Lett.* **116**, 161110 (2020).
- [37] <http://langsrv.astro.cf.ac.uk/RSESpherical/RSESpherical.html>.
- [38] S. V. Lobanov, W. Langbein, and E. A. Muljarov, Resonant-state expansion of three-dimensional open optical systems: Light scattering, *Phys. Rev. A* **98**, 033820 (2018).
- [39] L. Bi, W. Lin, Z. Wang, X. Tang, X. Zhang, and B. Yi, Optical modeling of sea salt aerosols: The effects of nonsphericity and inhomogeneity, *J. Geophys. Res.: Atmos.* **123**, 543 (2018).
- [40] I. Karanasiou, N. Uzunoglu, and C. Papageorgiou, Towards functional noninvasive imaging of excitable tissues inside the human body using focused microwave radiometry, *IEEE Trans. Microwave Theory Tech.* **52**, 1898 (2004).
- [41] Y. Li, L. Rao, R. He, G. Xu, Q. Wu, W. Yan, G. Dong, and Q. Yang, A novel combination method of electrical impedance tomography inverse problem for brain imaging, *IEEE Trans. Magn.* **41**, 1848 (2005).
- [42] J. Sun and G. D. Egbert, A thin-sheet model for global electromagnetic induction, *Geophys. J. Int.* **189**, 343 (2012).
- [43] <http://doi.org/10.17035/d.2022.0162370874>.
- [44] D. Braunstein, A. M. Khazanov, G. A. Koganov, R. Shuker, and E. P. Gordov, Location and width of morphology-dependent resonances in microspheres, in *ICONO '95: Fundamentals of Laser-Matter Interaction*, edited by K. N. Drabovich and N. I. Koroteev, International Society for Optics and Photonics Vol. 2796 (SPIE, Bellingham, Washington, 1996), pp. 296–304.
- [45] G. Roll and G. Schweiger, Geometrical optics model of Mie resonances, *J. Opt. Soc. Am. A* **17**, 1301 (2000).
- [46] J. R. Probert-Jones, Resonance component of backscattering by large dielectric spheres, *J. Opt. Soc. Am. A* **1**, 822 (1984).
- [47] S. Neale and E. A. Muljarov, Resonant-state expansion for planar photonic crystal structures, *Phys. Rev. B* **101**, 155128 (2020).
- [48] L. J. Armitage, M. B. Doost, W. Langbein, and E. A. Muljarov, Resonant-state expansion applied to planar waveguides, *Phys. Rev. A* **89**, 053832 (2014).
- [49] J. P. Dahl and M. Springborg, The Morse oscillator in position space, momentum space, and phase space, *J. Chem. Phys.* **88**, 4535 (1988).